Atmospheric Research 90 (2008) 10–32

Contents lists available at ScienceDirect

Atmospheric Research

journal homepage: www.elsevier.com/locate/atmos

The remarkable wide range spatial scaling of TRMM precipitation

S. Lovejoy[a,b,*], D. Schertzer[c,d], V.C. Allaire[a]

[a] *Physics, McGill University, 3600 University St., Montreal, Quebec, Canada*
[b] *Centre GEOTOP UQAM/McGill, Université du Québec à Montréal, Montréal, Canada*
[c] *Université Paris-Est, ENPC/CEREVE, 77455 MARNE-LA-VALLEE Cedex, France*
[d] *Météo France, 1 Quai Branly, 75007 Paris, France*

ARTICLE INFO

Article history:
Received 3 August 2007
Received in revised form 11 February 2008
Accepted 18 February 2008

Keywords:
Precipitation
Satellite radar data
Scaling
Multifractals
Cascades

ABSTRACT

The advent of space borne precipitation radar has opened up the possibility of studying the variability of global precipitation over huge ranges of scale while avoiding many of the calibration and sparse network problems which plague ground based rain gage and radar networks. We studied 1176 consecutive orbits of attenuation-corrected near surface reflectivity measurements from the TRMM satellite PR instrument. We find that for well-measured statistical moments (orders $0<q<2$) corresponding to radar reflectivities with $dBZ<57$ and probabilities $>10^{-6}$, that the residuals with respect to a pure scaling (power law) variability are remarkably low: ±6.4% over the range 20,000 km down to 4.3 km. We argue that higher order moments are biased due to inadequately corrected attenuation effects. When a stochastic three — parameter universal multifractal cascade model is used to model both the reflectivity and the minimum detectable signal of the radar (which was about twice the mean), we find that we can explain the same statistics to within ±4.6% over the same range. The effective outer scale of the variability was found to be 32,000±2000 km. The fact that this is somewhat larger than the planetary scale (20,000 km) is a consequence of the residual variability of precipitation at the planetary scales. With the help of numerical simulations we were able to estimate the three fundamental parameters as $\alpha\approx1.5$, $C_1=0.63\pm0.02$ and $H=0.00\pm0.01$ (the multifractal index, the codimension of the mean and the nonconservation parameter respectively). There was no error estimate on α since although $\alpha=1.5$ was roughly the optimum value, this conclusion depended on assumptions about the instrument at both low and high reflectivities. The value $H=0$ means that the reflectivity can be modeled as a pure multiplicative process, i.e. that the reflectivity is conserved from scale to scale. We show that by extending the model down to the inner "relaxation scale" where the turbulence and rain decouple (in light rain, typically about 40 cm), that even without an explicit threshold, the model gives quite reasonable predictions about the frequency of occurrence of perceptible precipitation rates.

While our basic findings (the scaling, outer scale) are almost exactly as predicted twenty years ago on the basis on ground based radar and the theory of anisotropic (stratified) cascades, they are incompatible with classical turbulence approaches which require at least two isotropic turbulence regimes separated by a meso-scale "gap". They are also incompatible with classical meteorological phenomenology which identifies morphology with mechanism and breaks up the observed range 4 km–20 000 km into several subranges each dominated by different mechanisms. Finally, since the model specifies the variability over huge ranges, it shows promise for resolving long standing problems in rain measurement from both (typically sparse) rain gage networks and radars.

1. Introduction

Rain is highly turbulent and displays enormous variability over huge ranges of space-time scales. Indeed, starting in the

---

[*] Corresponding author. Physics, McGill University, 3600 University St., Montreal, Quebec, Canada.
E-mail address: lovejoy@physics.mcgill.ca (S. Lovejoy).

0169-8095/$ – see front matter © 2008 Elsevier B.V. All rights reserved.
doi:10.1016/j.atmosres.2008.02.016

1980s, a large number of papers reported that over various ranges rain displayed scaling properties; (Lovejoy, 1982; Lovejoy and Schertzer, 1985; Schertzer and Lovejoy, 1987; Hubert and Carbonnel, 1988; Hubert and Carbonnel, 1989; Gupta and Waymire, 1990; Olsson et al., 1990; Hubert and Carbonnel, 1991; Gupta and Waymire, 1991; Hubert et al., 1993; Olsson et al., 1993; Kumar and Foufoula-Georgiou, 1993; Tessier et al., 1993; Hubert, 1995; Hubert and Carbonnel, 1988; Kumar and Foufoula-Georgiou, 1993; Schertzer and Lovejoy, 1987; Olsson, 1995; Tessier et al., 1996; Harris et al., 1996; Over and Gupta, 1996c; Veneziano et al., 1996; Menabde et al., 1997; Bendjoudi et al., 1997; Tessier et al., 1996; De Lima, 1998; Deidda, 2000; Deidda et al., 2004; Lovejoy et al., 2003; Lovejoy and Schertzer, 2006a); for an early review see Lovejoy and Schertzer (1995). In scaling processes, a scale invariant mechanism repeats scale after scale, the generic model – first studied in turbulence – being the cascade process. In turbulent cascades, starting at a large outer scale the variability builds up scale by scale leading to extreme small scale multifractal variability of roughly the observed type. In order to demonstrate the cascade nature of rain and to estimate the corresponding statistical exponents, one can attempt to "invert" the cascade by successively removing the variability by degrading the resolution. An early analysis of this type from data taken from a 10 cm wavelength radar over a three week period in Montreal at 1 km spatial resolution is shown in Fig. 1. These high quality radar reflectivities demonstrate the excellent multiscaling of rain over the range 1 km to 128 km. As can be seen from the figure, extrapolation of the lines to the scale where the variability vanishes (where the lines cross at large scales) indicates that the data is very accurately explained by a cascade with an "effective" outer scale of ≈32,000 km. As explained in Lovejoy and Schertzer (2006a) and Lovejoy et al. (2001) – where very similar results were obtained for visible and infra red cloud radiances – the fact that this scale is a bit larger than the largest distance on the earth (20,000 km) is due to nonlinear interactions with other fields, so that rain is variable even at planetary scales. In a recent publication (Lovejoy et al., submitted for publication), these results have been extended using TRMM visible, infra red and passive microwave radiances (ten channels in all) showing that the latter are accurately scaling with outer scales in the range 5000–20,000 km (depending somewhat on the wavelength). These results are not too surprising when we recall that cascades were initially developed as a model of fully developed turbulence and are now known to be extremely general. Recently (work in progress with J. Stolle), we have shown that numerical weather models and re-analyses (ERA40) accurately follow cascade statistics from nearly 20,000 km down to a small scale where they are cut-off by (hyper) viscosity at ≈100 km. Therefore it now seems that if the data fail to have cascade structures, then they are likely to be incompatible with the numerical models.

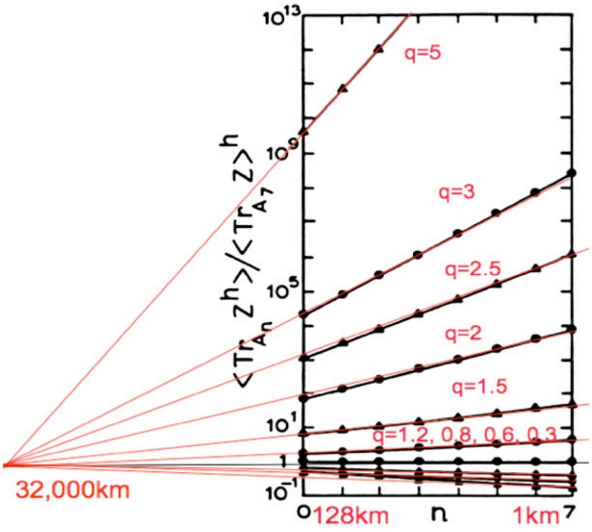

Fig. 1. The normalized radar reflectivity from 70 Constant Altitude *Z* LOg Range (CAZLOR) maps at 3 km altitude from the McGill weather radar (10 cm wavelength, 0.96° angular resolution with, 1 km pulse length). All the 70 CAZLORs taken over a three week period were used. The maximum range was determined by the requirement of keeping the resolution to 1 km and the curvature of the earth. The straight lines indicate multiscaling behaviour, the slopes are the $K(q)$ function (c.f. Eq. (1)). The straight lines (added from the original figure in Schertzer and Lovejoy, 1987) show that the variability can be explained if the effective outer scale of the cascade is about 32,000 km (this is not a fit, it is the value estimated on the TRMM data below). The notation in the original figure is $n = \mathrm{Log2}\ L_{\mathrm{ref}}/L$ with $L_{\mathrm{ref}} = 128$ km and $h = q$ and the ordinate is the normalized moment $M_q = \langle Z_l^q\rangle / \langle Z_1\rangle^q$.

Replacing the extrapolations in Fig. 1 with real large scale data has proved to be very difficult. One reason is that for a single radar at 1 km resolution, the upper limit of 128 km in Fig. 1 is about the largest possible. However even at lower resolutions, the curvature of the earth prevents single radars from covering scales of more than a few hundred kilometers. In principle, the large radar networks that were developed in both North America and Europe in the 1990s could overcome this problem, but in practice, there are many obstacles in using them for large scale studies. These include nontrivial intercalibration problems, range dependencies, inter-radar "boundary" problems and others. Similarly, global in situ raingage networks are sparsely distributed over fractal sets (Lovejoy et al., 1986; Tessier et al., 1994). However, when this effect is statistically removed, they are indeed found to show large scale scaling (Tessier et al., 1993) although with relatively poor spatial resolution compared to TRMM. Other indirect methods of inferring the type of large scale statistical variability of rain include the study of the nonlinearly related cloud radiances (e.g. Lovejoy et al., 2001).

In the 1990s, a new technology – satellite precipitation radar – for the first time yielded precipitation measurements with near uniform coverage from 4.3 km resolution to planetary scales (250 m in the vertical, swath width 220 km, 13.8 GHz), covering the region ±38° latitude: the Tropical Rainfall Measuring Mission (TRMM). Due to the narrow swath the resolution is quite uniform varying between a maximum of 4.8 km and minimum of 4.1 km. Although many problems plague its use for quantitative rain rate estimates, the reflectivity factor is quite well estimated; the main problem being the difficulty in correcting for beam attenuation at high rain rates (TRMM Precipitation Radar Team, 2005), and the inability to detect low reflectivities (roughly those below twice the mean, see below). In this paper we use over 1100 orbits of the attenuation-corrected, near-surface TRMM reflectivities (product 2A25), to determine the statistical properties of reflectivity over a range of factor >4000 in scale. With the help of stochastic cascade models of rain and a simple threshold model for the minimum detectable signal, we show that rain is remarkably scale invariant over the entire observed range.

2. Data analysis

The TRMM satellite was launched at the end of 1997 and is still operational after over 54,000 orbits. In this paper we primarily analyzed 1176 (near continuous) data spanning the period Jan 1 1998–March 16 1998; i.e. 75 days; Fig. 2 shows an example. The data quality was generally very high; only 50 orbits were put aside due to excessive fractions of missing data. Perhaps the most striking feature of Fig. 2 is the extreme sparseness of the raining regions. For example, over this period, the mean reflectivity Z was 53 ± 34 mm^6/m^3 (17.2 ± 2.1 *dBZ*) while only $3.51 \pm 1.4\%$ of the pixels were above the minimum detectable signal; see Fig. 3A for a graphical display (the standard deviations indicate the orbit-to-orbit spread about the overall means). Although things are complicated by the attenuation correction, to a first approximation (discussed in more detail below), no signal below about double the mean was detectable (≈20 *dBZ*; this is close to the figure of 20.8 *dBZ* given in TRMM Precipitation Radar Team, 2005). Applying the standard Marshall–Palmer relation, $Z = aR^b$ with $a = 200$, $b = 1.6$, at 4.3 km resolution we find this corresponds to a mean rain rate (R) of 0.085 ± 0.04 mm/h = 2.49 mm/day in raining regions (see Fig. 3B). Note that the values $a = 300$, $b = 1.4$ are used in the version 4 TRMM rain rate algorithm and the rain rate in the 2A25 algorithm uses variable a, b values depending on a complex precipitation classification scheme (TRMM Precipitation Radar Team, 2005); however these differences will not change the following rough estimates by much.

We can already note an important consequence of scale: if we convert the large (orbital/planetary scale) mean Z into nominal R using the Marshall–Palmer relation, we obtain the much larger value 0.44 mm/h. This large bias factor 0.44/0.085 = 5.2 is purely a consequence of the different resolutions (scale ratio >4000) coupled with the nonlinear Z–R relation which is defined at the unique (subjective) radar resolution. Since such deterministic mapping of reflectivities onto rain rates can at most be valid at a single resolution, this underlines the need for the development of resolution independent radar calibration techniques (see the discussion below; this statement is also true about the complex TRMM rain rate retrieval algorithms which will also suffer from the same problem). In comparison, Chiu and Shin (2004) find 2.30 mm/day for the entire period Jan. 1998–Dec. 2003 for the calibrated TRMM radar rain estimates. This is also very close to the radar estimated values for Montreal (3.07, 2.46 mm/day in 1976, 1977 respectively) and for the tropical Atlantic (GATE experiment 2.76 mm/day) so that the results of Fig. 1 are apparently comparable to those of TRMM (Lovejoy and Austin, 1979). Neglecting coherent scattering effects and the effect of the attenuation corrections, the radar measures the reflectivity factor Z which is the density of V^2 within the radar pulse volume (V is a drop volume). In comparison, the rain rate R is the density of Vw where w is the vertical drop fall speed. Therefore, we expect the Z–R relation to be only statistical in nature and – due to the spatial scaling of rain – it will be resolution dependent (see e.g. Lovejoy et al., 1996). In this paper, we therefore avoid converting Z to R taking the view that the TRMM Z is a well estimated empirical field which is strongly nonlinearly coupled with precipitation: while the scaling exponents of Z and R will be different, the scaling ranges will be essentially the same.

In order to analyze the reflectivities and determine their scaling exponents, we systematically degraded the data to lower and lower resolutions by spatial averaging. This simple "trace moment" technique is motivated by cascade models that build up the variability from large to small scales; the degrading can be viewed as an attempt to invert this process. If the external scale of the cascade (the largest scale of the

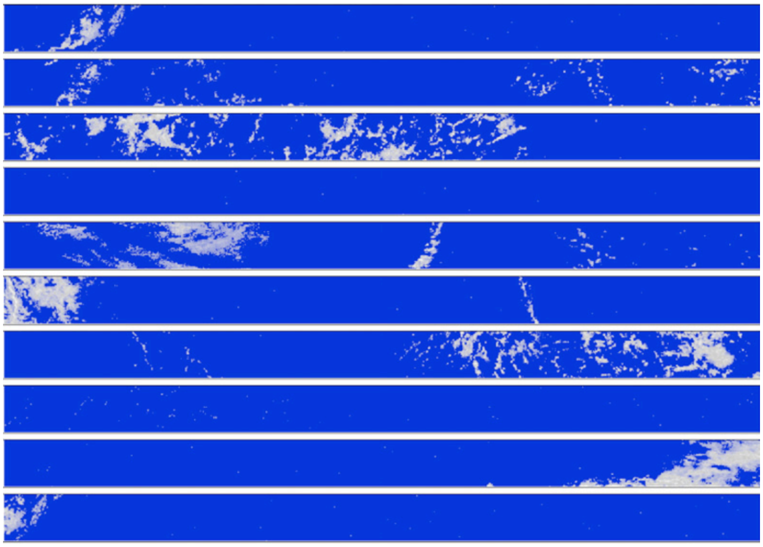

Fig. 2. This shows a single orbit (49 pixels across, 9300 pixels long, broken into 10 segments and displayed consecutively one on top of the other) with false colors according to log Z, blue indicating signal below the detection threshold. (For interpretation of the references to color in this figure legend, the reader is referred to the web version of this article.)

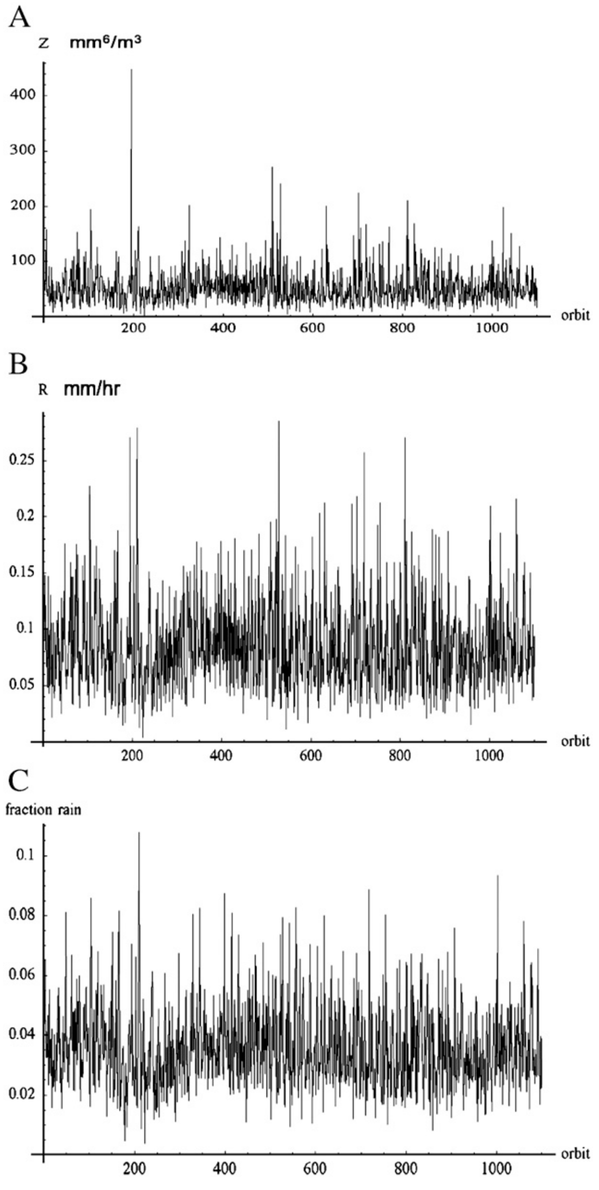

Fig. 3. A: This shows the mean reflectivity for each orbit (area/orbit≈9×107 km^2). B: This shows the nominal rain rate obtained by applying the Marshall–Palmer relation $Z=200R1.6$ at the smallest resolution (4.3 km) and then averaging over an entire orbit. C: This shows the mean fraction of area above the minimum attenuation-corrected signal for each orbit.

variability) is denoted by L_{eff}, the (degraded) resolution by L and the scale ratio by λ' then we expect:

$$\langle Z_{\lambda'}^{q}\rangle = \lambda'^{K(q)}\langle Z_1\rangle^{q};\quad \lambda' = L_{\mathrm{eff}}/L \tag{1}$$

where <Z$_1$> is the ensemble (i.e. climatological) mean (here $<Z_1>=53$ mm^6/m^3; the subscript “1” refers to the largest spatial scale ratio $\lambda'=1$, hence spatial scale L_{eff}), $K(q)$ is the moment scaling exponent. The reason for using the prime for the scale ratio is that in our case, L_{eff} is *a priori* an unknown empirically determined parameter; in practice, we use instead a reference scale conveniently taken as the largest great circle distance on the earth: $L_{\mathrm{earth}}=20{,}000$ km. We therefore introduce the unprimed scale ratio:

$$\lambda = \frac{L_{\mathrm{earth}}}{L} \tag{2}$$

and define:

$$\lambda_{\mathrm{eff}} = L_{\mathrm{earth}}/L_{\mathrm{eff}} = \lambda/\lambda' \tag{3}$$

For the normalized moments M_q we therefore expect:

$$M_q = \frac{\langle Z_{\lambda'}^{q}\rangle}{\langle Z_1\rangle^{q}} = \lambda'^{K(q)} = \left(\frac{\lambda}{\lambda_{\mathrm{eff}}}\right)^{K(q)} \tag{4}$$

Equivalently, rather than using (normalized, nondimensional) statistical moments, the statistics of the process can be specified by their probability distributions:

$$\Pr\left(Z_{\lambda'} > \lambda'^{\gamma}\right) \approx \lambda'^{-c(\gamma)} \tag{5}$$

where “≈” means equality to within slowly varying factors, $\gamma=\log(Z_{\lambda'}/<Z_1>)/\log\lambda'$ is the “order of singularity” corresponding to the field value $Z_{\lambda'}$ and $c(\gamma)$ is the codimension function, the exponent that specifies the probabilities at each scale. The moment and probability descriptions of the statistics are equivalent; the exponents are related by the following Legendre transformation:

$$\begin{aligned} c(\gamma) &= \max_{q}(q\gamma - K(q)) \\ K(q) &= \max_{q}(q\gamma - c(\gamma)) \end{aligned} \tag{6}$$

(Parisi and Frisch, 1985). Eq. (6) implies that there are one-to-one relations between the orders of singularity and moments:

$$\gamma = K'(q);\quad q = c'(\gamma) \tag{7}$$

These relations imply that there is a unique field value that gives the dominant contribution to each qth order moment.

Note that the above $K(q)$, $c(\gamma)$ framework is called the “codimension multifractal formalism” (Schertzer and Lovejoy, 1987) and is particularly advantageous when applied to stochastic multifractals. In comparison, there is a $\tau(q)$, $f(\alpha)$ “dimension multifractal formalism” (Halsey et al., 1986) which was developed for (deterministic) systems such as strange attractors. While the former is based on the statistics of densities of measures (the field values, here the reflectivity per unit volume), the latter is based on measures (i.e. integrals of the field values, here the total reflectivity in a volume). The relation between the two notations is $\tau(q)=(q-1)D-K(q)$, $\alpha=D-\gamma$, $f(\alpha)=D-c(\gamma)$ where D is the dimension of the observing space. The advantage of the codimension formalism is that the basic exponents K, c are independent of D, in particular, they are well defined (generally finite) as D becomes infinite (such as for the stochastic cascade processes discussed below). In the rain literature there is yet another notation (Over and Gupta, 1996a; Gebremichael et al., 2006) which uses a scale ratio λ_n equal to $1/\lambda'$ and with an exponent $\tau_{\mathrm{OG}}(q)=-\tau(q)$.

Due to technical reasons (essentially the slowly varying prefactors in Eq. (5)), it turns out to be somewhat simpler to analyze the moments (Eq. (1)) rather than the histograms (see however Section 4.4.2). Fig. 4A shows the result for all the orbits (January–March 15 1998) showing the excellent scaling for $0\le q<3$ for the normalized moments M_q. The most striking

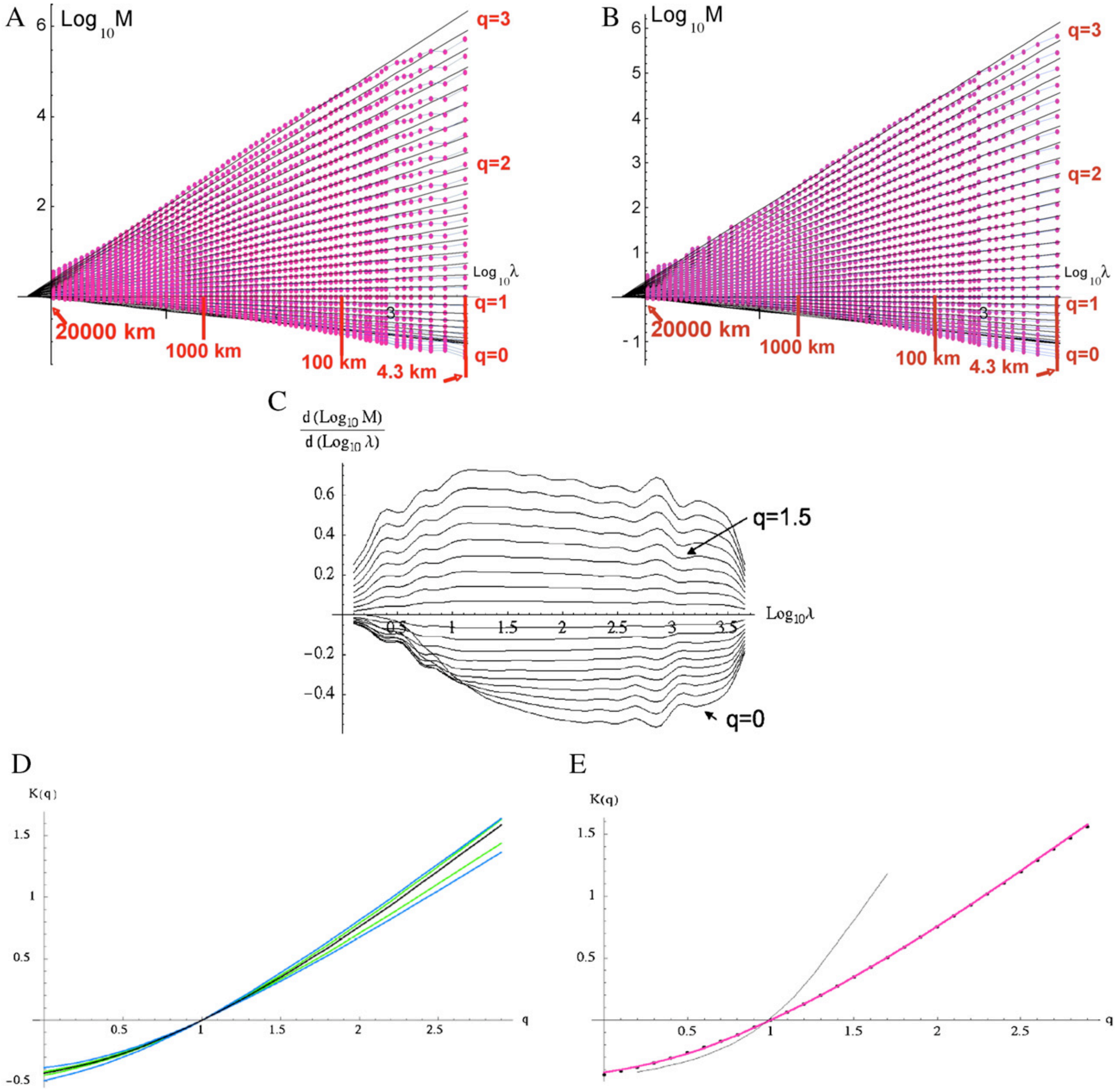

Fig. 4. A: This shows the logarithm of the moments $M=\langle Z_\lambda^q\rangle/\langle Z_1\rangle^q$ of reflectivity normalized by the mean over all the orbits $<Z_1>$). Each curve is for a different order moment with q decreasing from 3 at the top to 0 at the bottom in steps of 0.1. The black lines are linear regressions. $\lambda=L_{\mathrm{earth}}/L$ where L is the resolution, $L_{\mathrm{earth}}=20{,}000$ km is the largest great circle distance between two points on the earth. We have placed reference lines forced to pass through the estimated effective outer scale of 32,000 km. B: The same as panel A except that the field being analyzed is the absolute gradient of Z at the finest (4.3 km) resolution (δZ_λ). C: The logarithmic derivative of the moments M of δZ_λ with respect to scale ratio λ. (i.e. the slopes of graphs in panel B). These were smoothed with a moving window resolution $\log_{10}\lambda=0.2$. Each line corresponds to q increasing form 0 to 1.9 in steps of 0.1 (bottom to top). The main deviations from constancy are at the extreme ends and at low q. D: This shows the $K(q)$ estimated from the slopes of the trace moment. The black line is from the mean all the orbits; the outside blue lines show the spread of the $K(q)$ calculated on single orbits, the green, calculated on single days (the spread indicates one standard deviation variations). For clarity the means for the single orbit and daily averages are not shown; they are half way between the corresponding upper and lower bounds. From the slope at $q=1$ we obtain an estimate of the codimension of the mean ($C_1=K'(1)$). The zero rain areas appear to have a codimension of about $C_s=-K(0)=0.42$, although this is shown to be an artifact of the minimum detectable signal (Section 3). E: The thick red line is the $K(q)$ function estimated from the TRMM data reflectivities, the dots are from the absolute gradient reflectivities (δZ), and the black line is from the land-based radar data (Fig. 1, replotted from analyses in Schertzer and Lovejoy, 1987). (For interpretation of the references to color in this figure legend, the reader is referred to the web version of this article.)

aspect of the figure is the remarkable straightness of the lines — over a factor of >4000 in scale, this extends the land-based results (Fig. 1) to planetary scales. It indicates that weak and strong events (small and large q respectively) are indeed accurately scaling over the range (we quantify these statements below). To our knowledge, this is the first direct evidence that the scaling of any atmospheric field extends to planetary scales (the scale by scale deviations are quantified in Section 3.2). This conclusion is reinforced by Fig. 4B which shows the same analysis obtained by replacing the reflectivity by the absolute gradient of the reflectivity at the highest resolution (and then degrading the latter to an intermediate scale ratio λ the result denoted δZ_λ). Again, the power law form is extremely well followed; we shall see that the result is almost identical, we also return to this below. A rather sensitive way to check the linearity of the graphs in Fig. 4A and B is to plot the logarithmic derivative as a function of $\log_{10}\lambda$. This is done in Fig. 4C for the δZ_λ analysis. We see that with the exception of the extreme low and high λ, the derivatives are very flat corresponding to pure power law behaviour. For $q>1$ (the points above the axis with $K(q)>0$), only when the resolution of the radar is approached — or the size of the earth are the deviations important. For $q<1$ we see that the scaling is less good; we explain this below.

From the point of view of precipitation research, this highly accurate wide range scaling is at odds with the assumptions of the phenomenological approaches and models of rain and rain systems. These approaches break the scale range into subranges each with qualitatively different dynamics (some authors even go to the extreme of subdividing the range into factors of 2 in scale). However since the precipitation field is strongly nonlinearly coupled to the dynamics (particularly the convergence), the implications of Fig. 4A and B go beyond precipitation: it is hard to escape the conclusion that atmospheric dynamics are also scaling over the same wide range. Indeed in a recent paper we show that TRMM radiances similarly display wide range scaling: the visible, thermal IR and TRMM data at 2.2 km also have excellent scaling – as do the TRMM passive microwave channels at somewhat lower resolutions – although with different exponents and slightly smaller outer scales; 10 channels in all (Lovejoy et al., submitted for publication). This is consistent with the much smaller (29 scene) geostationary IR data set analyzed in (Lovejoy et al., 2001) and (Lovejoy and Schertzer, 2006a) which covered a 5000×5000 km zone over the Pacific. Over the range 10–5000 km, these TRMM sensors — which don't suffer from the minimum detectable signal problem of the radar — nor from attenuation — have mean absolute residual with respect to pure power law scaling (i.e. Eq. (4)), moments $q<2$ of around ±0.5% for the visible and Infra red and ±1.5% for the passive microwave channels. Finally the analysis of a Canadian global numerical weather model (GEMS) and the ERA40 reanalysis data shows that they also have remarkable cascade structures, i.e. they also respect Eq. (4) for the temperature, wind and other fields over planetary down to the model (hyper) viscous scales of about 100 km (work in progress with J. Stolle).

To understand what is "being cascaded", consider first the visible and infra red radiances which have cascade parameters very close to those of passive scalars (in particular, the H parameter discussed below is near the theoretical value of 1/3 corresponding to a spectrum near $k^{-\beta}$ where k is a wavenumber; ignoring intermittency the spectral exponent $\beta=1+2H-5/3$). In this case the basic cascaded quantity is likely to be the scale by scale conserved liquid water variance flux which (with the energy flux) determines the statistics of the liquid water density. For the reflectivity factor (which unlike the rain rate, does not depend on the vertical velocity field), it seems likely that it is the same basic cascade but highly thresholded i.e. only the extreme high liquid water density contributes. In Lovejoy and Schertzer (in press) it is argued that at large enough scales, this thresholding effectively reduces the H value to zero. This type of mechanism may explain the recent cloud reflectivity observations of Hogan and Kew (2005) where a transition was found from roughly $H\approx 1/3$ (i.e. $\beta\approx 5/3$) at small scales to $H\approx 0$ (i.e. $\beta\approx 1$) at large scales. This type of transition in the H (or more or less equivalently, in the spectral exponent β) is similar to that found in high resolution rain gauge series analyzed in Fraedrich and Larnder (1993).

We can use Fig. 4A to estimate the $K(q)$ from the slopes of linear regressions, Fig. 4D shows the result. In the figure, we compare the $K(q)$ for all the orbits with those calculated from individual orbits (the blue lines show orbit to orbit variability), and from daily statistics (16 orbits) indicated by the green lines. We see that the estimates of $K(q)$ are very robust although – and this is theoretically expected – the $K(q)$s are slightly different for $q>2$ see Section 4.3 for more discussion, and see Schertzer et al. (1993) for the theory of sample size effect on the estimation of multifractal cascade exponents (via both first and second order "multifractal phase transitions"). In Fig. 4E, we compare the analysis of Z_λ and δZ_λ showing that they are nearly identical; the smallness of their difference is significant and is discussed further in Section 4.2. Also shown in Fig. 4E is the $K(q)$ estimated from the land-based radar (from Fig. 1); for $q<1.2$ $K(q)$ is close to the TRMM values. As we discuss below, the difference between the land-based estimates and TRMM for $q>1.2$ is likely due to the effect of attenuation on TRMM, but not on the ground based estimates in Fig. 1 which use a 10 cm wavelength which is relatively unaffected by attenuation.

Adopting the convention $x^0=1$ for $x>0$, $x^0=0$ for $x=0$, we see that for the extreme $q=0$ value, the value $K(0)$ corresponds to the scaling of the regions with reflectivities exceeding the minimum detectable threshold, i.e. the "support". From the figure we can estimate the codimension C_s of the nonzero regions, the "support" of the precipitation; $C_s=-K(0)\approx 0.42$. This implies that the fractal dimension of the support in 2-D sections is $2\text{-}C_s=1.58$. We shall see below that this value is an artifact of the minimum detectable signal, a fact which explains the diversity of values reported in the literature (demonstrated also in the land-based estimates where we find $C_s\approx 0.47$; see Section 5.2.2 for a detailed discussion). From the figure, we can also directly estimate the codimension of the mean, C_1 from the slope $K'(1)$; we obtain $C_1=0.63$ implying that the fractal dimension giving the dominant contribution to the mean (c.f. Eq. (7)) on 2-D cross-sections is $2-0.63=1.37$ which is extremely sparse, a point to which we also return below. In comparison, the highly intermittent turbulent wind field has $C_1=0.07$; see Schmitt et al. (1992) and the review in Anselmet et al. (2001), and the TRMM visible and thermal IR channels are in the range $C_1=0.065$ to 0.084, the TRMM TMI (passive microwave) channels have C_1 in the range 0.10 to 0.26 (Lovejoy et al., submitted for publication). Using the value $C_1\approx 0.63$, the equation $Z_\lambda=\lambda'^{\gamma}\langle Z_1\rangle$ with $\gamma=C_1$ and the estimate (below) of the external scale ≈32,000 km, we find that the main contribution to the mean Z is $(32{,}000/4.3)^{0.63}=275$ times the mean, i.e. ≈14,600 mm^6/m^3 (=41.6 *dBZ*).

From Fig. 4A and B, we can see that the most significant persistent and wide ranging deviation from linearity is for the low q values (see the small – barely perceptible – low q curvature in Fig. 4A and B). Since thresholding is applied at a fixed resolution (4.3 km), it breaks the scaling giving rise to the curvature (see Larnder, 1995 for a detailed study of the effect of thresholds). There are also small deviations at higher q values (reflecting the difficulty in obtaining robust high order statistics). Finally there is a small curvature at the extreme factor of 4 or so in resolution (the far right of the graph ≈4–15 km). This is partially due to small scale quantification effects which were not taken into account in the analyses (points on the graph are shown every 0.05 in $\log_{10}\lambda$ even though for high λ corresponding to resolutions of 2 pixels, 3 pixels etc., the λ values are not so close together). In addition, since the corresponding land-based reflectivity moments (Fig. 1) show no curvature in the range 1–128 km, this small effect is partly due to a slight degree of oversampling (the data is slightly less variable than expected at the highest resolutions, this is a natural consequence of the somewhat arbitrary definition of radar resolution as the half beam power).

Without going further, we can quantify these deviations by estimating the mean absolute residuals:

$$\Delta = \overline{\quad} \log_{10}\left(\langle Z_\lambda^q\rangle / \langle Z_1\rangle^q\right) - \log_{10}\left(\left(/\lambda_{eff,q}\right)^{K(q)}\right). \tag{8}$$

For each q, Δ is determined by linear regression on Fig. 4A; the slope yields the theoretical $K(q)$ and the theoretical $\lambda_{\mathrm{eff},q}$ is determined from the intercept (slightly different for each q, hence the subscript). The overbar in Eq. (8) indicates averaging over the different resolutions λ over the full range of scales 20,000–4.3 km. Fig. 5 shows the result; we see that the scaling of both Z and δZ are within ±10% except at the very low q values most affected by the minimum detectable signal; the means for $0<q<2$ are ±6.4, ±4.6% respectively i.e. a little higher for Z than for δZ. This is already an impressive vindication of the scaling approach to atmospheric dynamics in general and rain models in particular. However we can use cascade models which include the threshold effect to give even more impressive agreement with the predictions of wide range scaling; the details are given in the next section. First, we can compare the thin pink and green lines in Fig. 5 for the residues of the Z statistics for the data and model respectively. We see that the magnitudes of the deviations as functions of q from perfect power law scaling are nearly identical, the effect of the threshold and normal statistical variability can explain almost all of the deviations. Second, we can compare the residuals between the data and the cascade model. These residuals are even smaller than the residuals with respect to pure scaling even though neither the slopes nor the intercepts are free parameters in the model. We should note here that as shown in Section 4.4.2, $q<2$ corresponds to $\gamma=K'(2)<\approx 0.85$ (Figs. 18, 19) and at the finest resolution to reflectivities ≤57 dBZ, i.e. to all except the most extreme (probability $\leq 10^{-6}$) events (Fig. 17).

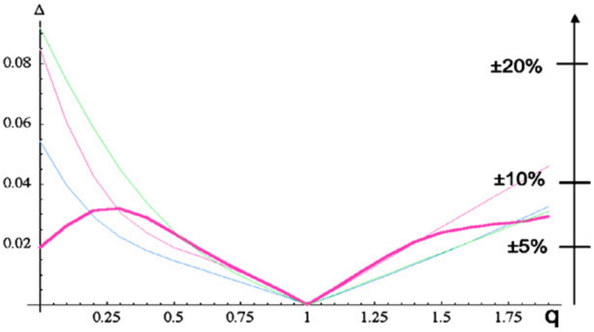

Fig. 5. This shows the absolute residuals D when the best fit to each line in Fig. 4A, B is used to estimate the moments (Z and δZ statistics, upper, pink and lower, blue respectively). Over the range of q values shown, the mean residues are 0.027, 0.018 respectively, i.e. ±6.4%, ±4.3%. The green line shows the residues from the model Z statistics (mean $D=0.026$ i.e. ±6.1%) which nearly identical to the data (red). Also shown (thick bottom line) is the residual of the Z analysis when compared to that of a multifractal cascade model with $a=1.5$, and a threshold $Z_t=2<Z_1>$ as discussed in the next section. The mean D is =0.0196, corresponding to ±4.6%. $D=0$ for $q=1$ since trivially $K(1)=0$. At the finest resolution, the range $0\leq q\leq 2$ roughly corresponds to all events with probabilities ≥10–6. (For interpretation of the references to color in this figure legend, the reader is referred to the web version of this article.)

3. Using multifractal simulations to test the cascade model

3.1. The cascade model

We have seen that the main deviations from the predictions of a pure cascade process are the low q curvature of the log of the moments with log of the scale and the fact that the lines for different q do not intersect at exactly the same effective outer scales. A priori, the simplest hypothesis for explaining these deviations is that they are scale breaking artifacts caused by the rather large minimum detectable signal: recall that this is of the order of twice the mean reflectivity (≈20 dBZ for the attenuation-corrected reflectivities; this corresponds to the minimum of the uncorrected signal; see TRMM Precipitation Radar Team, 2005). In order to quantitatively demonstrate that the thresholding is responsible for the breaks, we use an explicit multifractal cascade model coupled with a simple model for the effect of the minimum detectable signal; the signal below a minimum threshold is simply put to zero. Thresholding is only a crude model for the minimum detectable signal since the actual surface Z involves consideration of the statistics of electronic noise and attenuation corrections (see Section 4.4.2).

For the multifractal model, we exploit the fact that there are stable attractive cascade processes – a kind of “multiplicative central limit theorem” (Schertzer and Lovejoy, 1987; Schertzer and Lovejoy, 1997) – which leads to the following two-parameter multifractal universality classes:

$$K(q) = \frac{C_1}{\alpha - 1}(q^\alpha - q) \tag{9}$$

the Levy index $0\leq\alpha\leq 2$ quantifies the degree of multifractality; $\alpha=2$ corresponds to the “lognormal multifractal” (which – due to the divergence of high order statistical moments – is only approximately log–normal, see Section 4.4). Note that for $\alpha=1$, we have $K(q)=C_1 q\log q$, and for $\alpha<2$, $K(q)$ diverges for $q<0$. The “codimension of the mean” ($0\leq C_1$), quantifies the degree of sparseness of the reflectivity levels that give the dominant contribution to the mean; it turns out that this dominant contribution is $Z_\lambda/\langle Z_1\rangle \approx \lambda^{C1}$. The extreme case $\alpha=0$ (obtained in the limit $\alpha\to 0$ Eq. (4)) – where $K(q)$ becomes linear – is the monofractal “β model” (Frisch et al., 1978). This is the only model where in the limit $q\to 0$, we obtain $K(0)=-C_s$ corresponding to a fractal support (for $\alpha>0$, $K(0)=0$, the multifractal is space filling). Note that $K(q)$ is actually the cumulant generating function of log Z; $\alpha<2$ therefore corresponds to cumulant generating functions which are nonanalytic at the origin (i.e. at $q=0$), and therefore the cumulants of order $>\alpha$ diverge (in practice they will be very sensitive to very small values of Z i.e. those most affected by noise). These universal cascade processes are therefore outside of the restrictive framework considered by (Venugopal et al., 2006) who limited their attention to processes with strictly analytic cumulant generating functions.

We have already noted some exceptional universal multifractals: the (misnamed) $\alpha=2$ "log–normal" multifractal (which has – exceptionally – an analytic $K(q)$) and the $\alpha=0$ limit (the monofractal special case). In fact, it is useful to make a further qualitative distinction between the multifractals with unbounded and with bounded singularities, the $\alpha\geq1$ and $\alpha<1$ special cases respectively. The reason for this distinction is best understood by considering the relation between singularities and moments (Eq. (7)). Taking $K'(q)$ for the universal form (Eq. (9)), we see that for $\alpha\geq1$, as $q\to\infty$, $\gamma=K'(q)\to\infty$ (unbounded), whereas for $\alpha<1$, $K'(q)\to C_1/(1-\alpha)$ so that the singularities are bounded. As we shall see in more detail in Section 4 this difference loosely corresponds to multifractals dominated by high values or dominated by low values respectively. These theoretical statistics are valid for infinite sample sizes (and do not take into account the effect of cascade "dressing"; see Section 4.3), the unbounded cascade models are particularly sensitive to the size of the sample (number of orbits here), this is discussed in Section 4.3.

While the two-parameter form Eq. (9) is sufficient for a pure cascade process in which the turbulent fluxes are conserved from one scale to another, there is no compelling reason to assume that rain is (scale by scale) conserved. In general we must introduce a third universal multifractal parameter H; this is discussed in Section 4.3. However, since we conclude that empirically $H\approx0$, we ignore this complication for the moment.

Before going further, we must consider a basic problem; the nature of the zeroes, i.e. the value of the fractal codimension/dimension of the support of rain. This is a basic issue in the modeling of rain. One approach is to use two separate processes; a β model (i.e. a universal multifractal with $\alpha=0$) for the support and another cascade process to determine the distribution of rain rates on the support. Due to the longstanding lognormal phenomenology of rain (e.g. Lopez, 1979), a hybrid obtained as the product of (statistically independent) $\alpha=2$ and $\alpha=0$ models has been popular (e.g. Gupta and Waymire, 1993; Over and Gupta, 1996b; Gebremichael et al., 2006). An alternative which is both simpler and also takes into account the correlations between the support and the intensities, is to use a unique space filling model with a threshold at low rain rates below which we obtain truly zero rain rates. While the latter (unique process) model is more parsimonious, it has the disadvantage of yielding a scale break caused by the thresholding. On the other hand the hybrid β/log–normal model is perfectly scaling but yields a model with all the rain on a fractal support i.e. horizontal sections of raining regions cover a strictly zero area when the model is taken to the small scale limit. In practice, the model will be cut-off at a small decoupling scale where the turbulence and rain decouple (for light rain around 30–50 cm, see Lilley et al. (2006) and Lovejoy and Schertzer (in press) so that a finite value will result. However, in Section 4 we argue that given the observed extreme sparsity implied by $C_1=0.63$, that a threshold may only be needed at extraordinarily low rates (perhaps <1 mm/year) so that in practice the exact value of the threshold may not be so important. Recently (Lovejoy and Schertzer, in press), it has been argued that in actual fact the rain rate should be modeled as a compound multifractal — Poisson process whose mean (over the Poisson drop processes) is $R=\rho(w+v)$ where ρ, w are the (multifractal, turbulent) liquid water densities and vertical velocities respectively, and v is an appropriate mean drop relaxation (terminal velocity) field. Due to the Poisson conditioning, whenever the particle number density is very low, the probability of rain also becomes low; this acts as an effective threshold. In other words, a cascade model with threshold may be a theoretically justified approximation to real rain.

For the purposes of modeling the TRMM reflectivities, we can therefore exploit the extreme sparseness implied by $C_1=0.63$ and use space filling models ($\alpha>0$), with no additional model for the support. Because of the anticipated strong effect of the large minimum detectable signal on the low order (low q) statistics, and the potential effect of attenuation on the high order statistics, choosing the parameters of the model is somewhat delicate. For example, we must already verify on simulations that the naïve estimate $C_1=K'(1)$ is not biased by the minimum detectable signal; we find a change of only 0.02 which – according to simulations – is about the accuracy with which we can estimate C_1 with the given scale range and number of simulated orbits (10 here). In this way we estimate $C_1=0.63\pm0.02$ (in effect, we are not simply performing regressions but rather testing a family of stochastic models). However, if we attempt to use the second derivative $K''(1)$ to characterize the degree of multifractality of the process (as for example in Gebremichael et al., 2006), we find that the value is badly biased: the empirical $K''(1)\approx0.260$ is nearly the same as the (thresholded) model value ≈0.234, but it is much smaller than the unthresholded value ≈0.94). In other words, due to the spurious effect of the minimum detectable signal, $K''(1)$ is a factor $0.94/0.235\approx2.65$ too small; using $Z=aR^{b}$ with $b=1.4$ as in Gebremichael et al. (2006), we find the biased value $K_R''(1)=0.14$ which is indeed close to the values found in their Fig. 7. To determine the optimum parameters of the model, we use a "bootstrap" approach in which the parameters are first naively estimated, and then adjusted with the help of stochastic models which include the minimum detectable signal as well as the finite data sample effect.

Parameters which are fairly straightforward to estimate are $C_1=K'(1)=0.63$ and the mean $\langle Z_1\rangle=53$ mm^6/m^3; these were determined in advance. The fundamental universal multifractal parameter α as well as the external scale L_{eff} (and to some extent the minimum detectable signal Z_t) was determined by comparing the model to the results of simulations. In this context, it is relevant to note that the empirical values of (C_1, α) for Z reported in the literature are about (0.6, 0.5–0.6) in time, but are about (0.1–0.2, 1.4) in space (see Lovejoy and Schertzer, 1995; Lilley et al., 2006 for reviews). Although there is no necessity for the spatial and temporal parameters to be the same, the simplest space-time models predict the same α but possibly different C_1's and it is possible that the disagreement in the α values is an artifact due to the sensitivity of estimates to both poorly estimated low reflectivity levels and poorly estimated extremes (see Section 4.4). Finally we should note that if a Marshall–Palmer type power law relation exists between reflectivities and rain rates ($Z=aR^b$), then $\alpha_R=\alpha_Z$ and $C_{1R}=C_{1Z}b^{-\alpha}$ so that $C_{1Z}=0.63$ implies $C_{1R}=0.3$, 0.5 for $\alpha=1.5$, 0.5 respectively (using $b=1.6$). Using the temporal values (α_Z, C_{1Z})=(0.5, 0.6) we find (α_R, C_{1R})=(0.5, 0.5) which is in rough agreement with those in the literature from rain gauges whereas the spatial values (α_Z, C_{1Z})=(1.5, 0.6) lead to (α_R, C_{1R})=(1.5, 0.3) which have C_1 a little too large (c.f. 0.1–0.2), see Lilley et al. (2006).

For the TRMM data, aside from $<Z_1>$ and C_1, the optimum parameters were estimated to be $\alpha=1.5$, $H=0.00\pm0.01$, $Z_t\approx2<Z_1>$, $L_{\mathrm{eff}}=32{,}000\pm2000$ km. In Sections 4.1 and 4.2 we discuss in detail the justification for these H, and L_{eff} values including error estimates. However, we shall see that estimating α is not at all straightforward; and different α values imply slightly different thresholds Z_t so that for example $\alpha=0.5$ implies the larger optimum $Z_t\approx3$ $<Z_1>$. Due to the nontrivial attenuation correction and electronic noise, we shall see that the threshold model is not very precise so that from the data we may only conclude that $Z_t\approx2<Z_1>$. Hence, rather than attempting classical regression type analyses we will instead show that multifractal models with the basic exponents $C_1=0.63$, $\alpha=1.5$, and subsidiary parameters $L_{\mathrm{eff}}=32{,}000$ km, $Z_t=2<Z_1>$, $<Z_1>=53$ mm^6/m^3 yield very good fits to the empirical statistics, for all scales and moments $q<2$. We quantify the resulting deviations from the model (we discuss $q>2$ in Section 4.4.3); we also take the third basic exponent $H=0$, see below. Since the parameters have not been optimally fit, the quality (goodness of fit) of the underlying

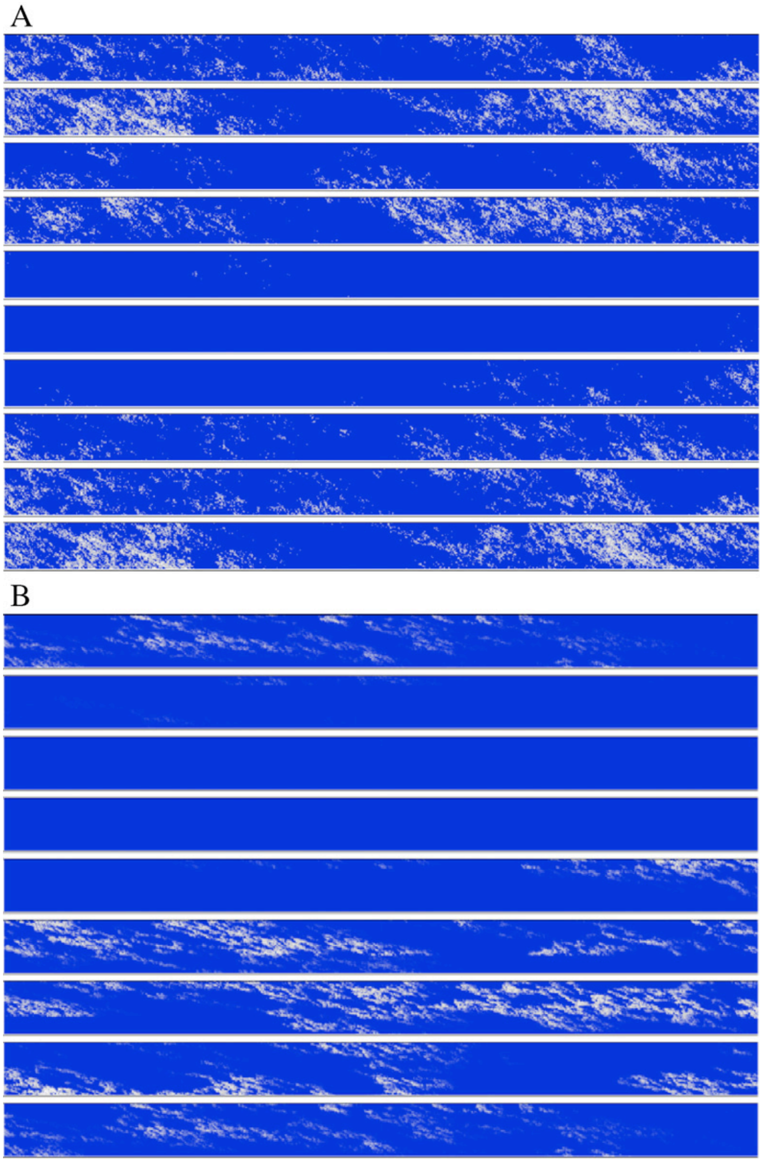

Fig. 6. A: A multifractal reflectivity simulation with the parameters $C_1=0.63$, $a=1.5$ with minimum detectable signal (blue background)=one half the mean showing a single strip 49 pixels wide and 2^{13} long divided into 8 consecutive pieces each 2^{10} long. To add realism, the model is of an anisotropic multifractal (using Generalized Scale Invariance, Lovejoy and Schertzer, 1985), hence the preferred directions. B: same but $a=0.5$, $C_1=0.63$. (For interpretation of the references to color in this figure legend, the reader is referred to the web version of this article.)

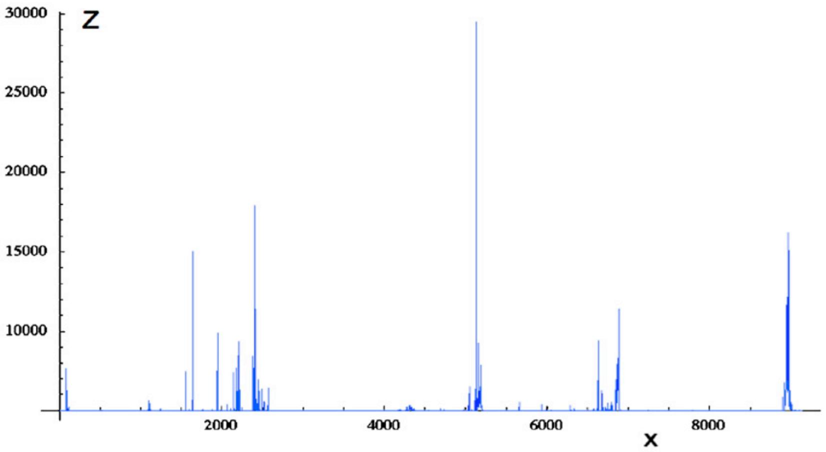

Fig. 7. This is a 1-D subsatellite section, one full orbit x coordinate in pixels (multiply by 4.3 for distances in km), y coordinate reflectivity factors in mm^6/m^3.

model will therefore be somewhat higher than that with the stated parameters. We shall see that the only parameter which is poorly estimated is α, and this is due to instrumental problems at both low and high *Z* values. This problem is probably best addressed with the help of the compound multifractal–Poisson drop model mentioned earlier which

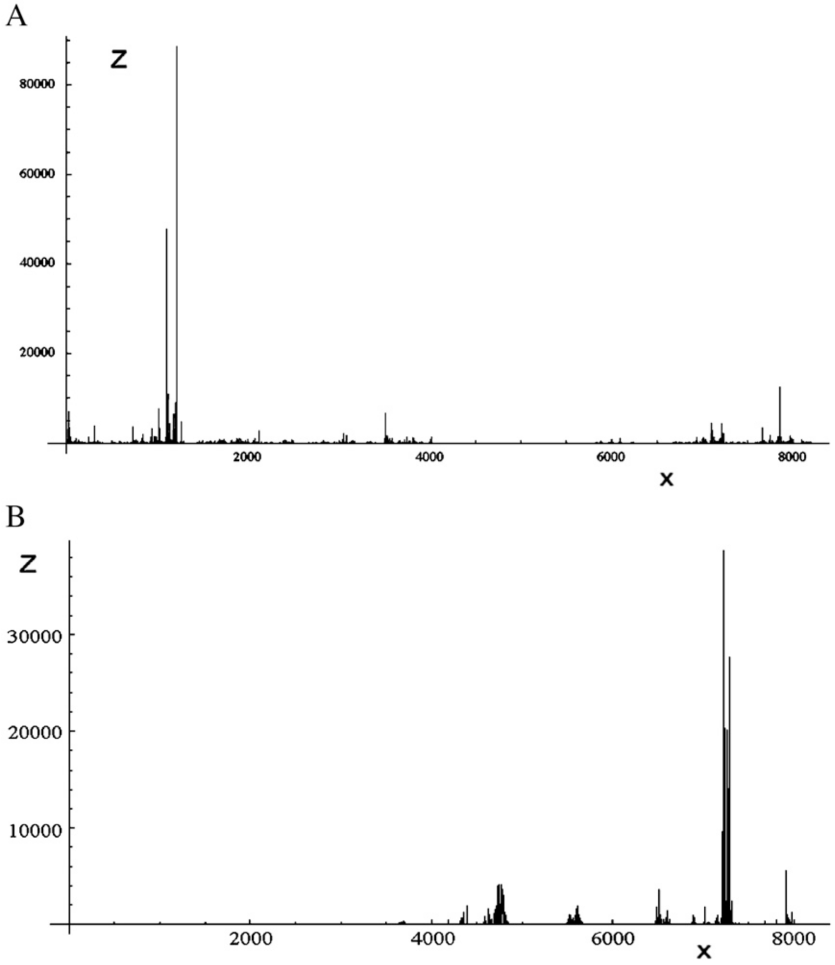

Fig. 8. A typical line 8192 pixels long through a simulation with α = 1.5, C1 = 0.63, the simulation is adjusted to have the same mean as the data (53 mm^6/m^3), same axes as Fig. 7. Note the extraordinary sparseness, variability. B: Same as A, but for α = 0.5, C1 = 0.63.

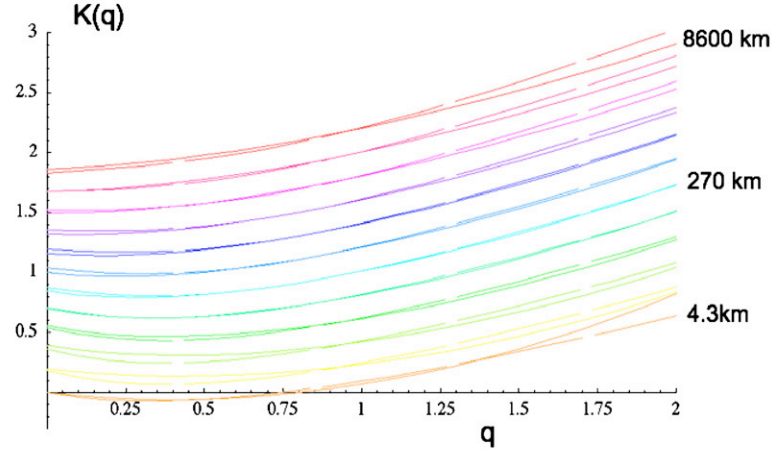

Fig. 9. Scale by scale comparison of the estimate of the exponent function K('(q) at scale λ' (Eq. (10)). The data is shown by the solid lines, the simulation by the dashed lines. Each curve is for increasing factors of two in resolution, and are offset by 0.2 in the vertical for clarity.

models the volumes and positions of individual drops yet at scales above the decoupling scale has cascade statistics.

3.2. Stochastic simulations — data inter-comparison, accuracy of the scaling

Fig. 6A and B shows a typical orbit simulation with the above-mentioned parameters, and Figs. 7,8A, B, compares typical 1-D (sub satellite) series and 1-D sections of a simulated orbits. The latter shows the extreme variability of the data and simulation. In Fig. 11 we compare the scaling of the normalized moments from 10 simulated orbits with those of the data (from Fig. 4A), with $Z_t=2{<}Z_1{>}$, ${<}Z_1{>}=53$ mm^6/m^3, $L_{\mathrm{eff}}=32{,}000$ km, $C_1=0.63$, $\alpha=1.5$.

We can see that the statistics of the simulation are very close to those of the data; there are various ways to quantify the small deviations. One way to do this is to consider the exponent scaling function defined in a scale by scale manner, i.e.

$$K_{\lambda'}(q) = \mathrm{Log}_{\lambda'}\left(\langle Z_{\lambda'}^{q}\rangle / \langle Z_1\rangle^{q}\right). \tag{10}$$

If the reflectivities are scaling (if they obey Eq. (1)), then $K_{\lambda'}(q)=K(q)$ i.e. it is independent of λ'. Here, we anticipate deviations particularly for small q, although we can verify how well the model reproduces the empirical behaviour; see Fig. 9.

We see that the main deviations are at the highest q values and the smallest and largest scales; the key point is that the low q deviations have been quite well reproduced (we quantify this below). High q deviations occur because of the high statistical variability of the processes; the data is also affected by attenuation (and the attenuation corrections are imperfect, especially at the high reflectivity levels which dominate the high q statistics, see Section 4.4.2). Since the simulation does not take this into account, it is not surprising that there are deviations here; three dimensional multifractal models (incorporating the scaling stratification of the reflectivity fields Lovejoy et al., 1987) could be used for simulating the attenuation and the attenuation correction procedure. Finally, the deviations from perfect power law scaling and the differences between the simulations and the data can also be displayed on contour plots of the scale by scale $K_{\lambda'}(q)$, see Fig. 10. Since perfect scaling means $K_{\lambda'}(q)$ is independent of λ', it leads to horizontal (flat) contours in Fig. 10. We see that as expected, the deviations are essentially for $q<1$ but are very similar for the simulations and data. We can also see that at $q\approx1.5$, the scaling is least affected by the low q and high q deviations.

Alternatively, we can directly compare the scale by scale moments for model and data, this is done in Fig. 11. We see that the curvature of the moments for low q is quite well reproduced. In order to quantify the residual data/model deviations, we calculate the residuals averaged over all scales as a function of q (Fig. 5). The figure shows that the model captures much of the low q curvature (we return to this in Section 4.4.1). For the moments $q<1.5$, and over the range of planetary down to 4.3 km, we see that the model reproduces

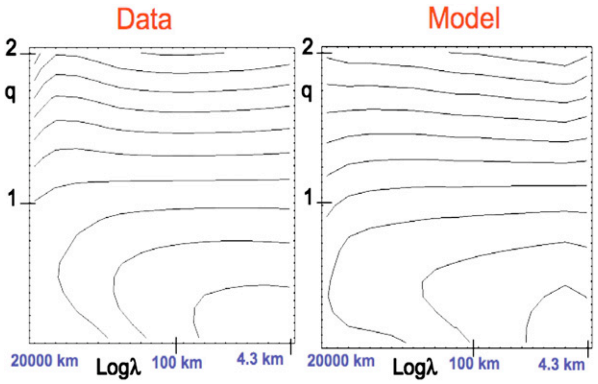

Fig. 10. This displays the scale λ estimated exponent $K_\lambda(q)$ shown here on a contour plot for the data (left) and simulation (right). Perfect power law scaling leads to $K_\lambda(q)$ independent of λ so that the contours are horizontal. Although the thresholding breaks the scaling it does so in nearly the same way for the simulation and data. The horizontal axis is $\log_2\lambda$ while the vertical axis is 10 ($q+0.1$); i.e. it ranges linearly from $q=0$ to $q=1.9$.

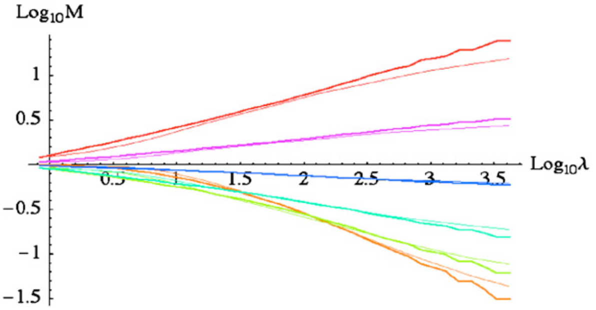

Fig. 11. This shows a scale by scale comparison of the normalized moments $M=\langle Z_\lambda^q\rangle/\langle Z_1\rangle^q$ as estimated by the simulation ($a=1.5$, $C_1=0.63$, $Z_t=2\langle Z_1\rangle$, $L_{eff}=$ 32,000 km (thick lines) and the data (thin lines) for $q=0$, 0.3, 0.6, 0.9, 1.2, 1.5. Note in particular that the low q curvature due to the thresholding is reasonably well reproduced.

the data to within ±4.6%. This means that to within this accuracy we can theoretically predict these moments at any scale over this range of a factor >4000 in scale.

4. Model parameter estimation

4.1. Discussion

Because of its far-reaching consequences for meteorology, the finding that rain can be accurately modeled by a scale invariant cascade over large ranges of scale is certainly the most important conclusion to be drawn from this study. However it would be a shame to leave things there; the TRMM data set also gives us a unique opportunity to resolve several longstanding qualitative problems in precipitation research, these include the nature of the zero rain rates (Section 5), and whether or not rain can adequately be modeled as a conserved (purely multiplicative) process (is H exactly zero?). It also allows us to quantitatively – and with unprecedented accuracy – estimate the external scale L_{eff} as well as the fundamental multifractal exponents α, C_1, H. In this section we therefore attempt to quantify these estimates. Readers not interested in these relatively technical details may skip to Section 5.

4.2. The external scale L_{eff}

A significant deviation from perfect cascade behaviour is the failure of the lines in Fig. 4A to intersect the abscissa at exactly the same scale i.e. the external scales apparently depend on q. Fig. 12A shows the comparison of the external scale as a function of statistical moments obtained for the data and the simulation (with $L_{eff}=32{,}000$ km). We see that the tendency of the data to have an external scale systematically smaller than 20,000 km for the $q<1$ and systematically larger than 20,000 km for $q>1$ is reproduced fairly accurately by the threshold model; note that the pure multifractal model (without threshold) shows a straight line at the level $\log_{10}\lambda_{eff}=\log_{10}(20{,}000/32{,}000)\approx-0.2$. We can exploit the fact that the scaling is very good for the $q=1.5$ moment in order to get a more accurate estimate of the external scale and to study its variability as we average over more and more orbits (Fig. 12B). We see that while the external scale varies greatly over single orbits with the mean L_{eff} for single orbits being somewhat below 20,000 km increasing to an asymptotic value of ≈32,000 km after ≈2 days. Since this is roughly the time it takes for the satellite to fully cover the globe between ±38°, this may explain why L_{eff} is underestimated for periods of only a few orbits. From this figure, we see that due to the large number of orbits, the statistical error in L_{eff} is very small, ultimately the error is a systematic one due to the effect of the threshold. From Fig. 12A, we can judge the systematic error from the slight slope in $\log_{10}\lambda_{eff}$ in the vicinity of $q=1.5$ (for both the data and simulation); it is about ±0.03 in $\log_{10}\lambda_{eff}$ i.e. about ±7% or ±2000 km. We can also see that the L_{eff} estimated by the gradients (Fig. 4B and C) is almost identical. Fig. 12B also shows that the random error in L_{eff} is much smaller than the systematic error found using the simulation Fig. 12A; we therefore conclude that $L_{eff}\approx32{,}000\pm2000$ km.

4.3. The degree of scale by scale conservation: the exponent H

Up until now we have assumed that the reflectivity is the direct result of a pure multiplicative cascade process. In as much as the pure multiplicative cascade simulations analyzed

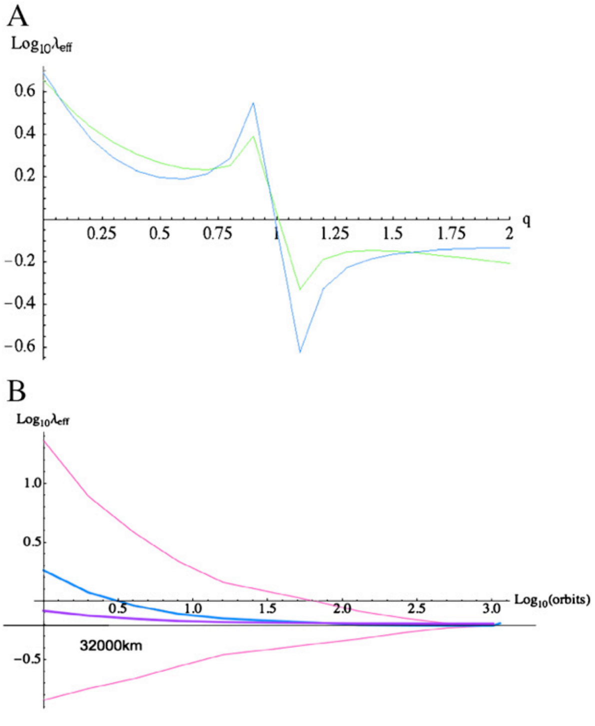

Fig. 12. A: This shows the effective outer scale as a function of q for the data (green) in Fig. 4A and for the simulation Fig. 8 (blue) $\lambda_{eff}=L_{eff}/L_{earth}$ with $L_{earth}=20{,}000$ km. This is estimated by making a linear regression of the log of the normalized moments (M) versus log scale and determining the intercept with the line $\text{Log}_{10}M=0$ (Eq. (4)). Since the slope $K(q)$ is exactly zero for $q=1$, for q near 1, the estimates are poor (in the above we simply put a straight line through the estimates for $q=0.9$ and $q=1.1$). Without threshold, the model outer scale 32,000 km corresponds to $\log_{10}\lambda_{eff}\approx-0.2$. The agreement of the blue and green curves shows that the low q behaviour is well modeled by the threshold. B: the effective outer scale as estimated by increasing numbers of orbits: blue is the mean, the pink are the one standard deviation error bars. The purple is the corresponding curve for the mean external scale as estimated by gradients (δZ). (For interpretation of the references to color in this figure legend, the reader is referred to the web version of this article.)

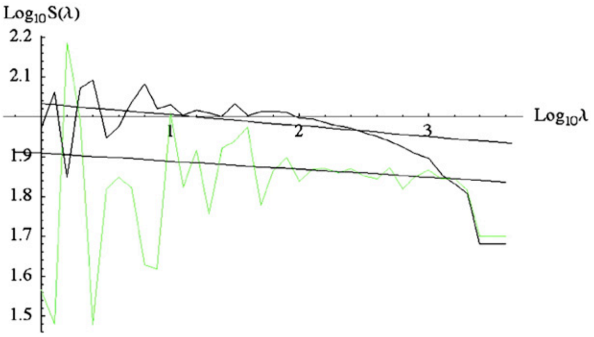

Fig. 13. The first order structure function for all the orbits, the absolute slope is an estimate of the nonconservation parameter H; $\lambda=L_{\mathrm{earth}}/\Delta x$. Black is the data, green is the simulation ($a=1.5$, $C_1=0.63$, $Z_t=2<Z_1>$, $L_{\mathrm{eff}}=32{,}000$ km, only 10 orbits, hence it is noisier at low λ). The lines have absolute slopes $H=0.034$, 0.027 respectively. (For interpretation of the references to color in this figure legend, the reader is referred to the web version of this article.)

in Section 3 accurately reproduce the observed statistical properties of the reflectivity, this assumption must be fairly realistic. Nevertheless, the mere existence of a scale invariant dynamical mechanism does not imply that the observable field is purely multiplicative, and this assumption must be quantitatively analyzed. To put this issue into perspective recall that the prototypical turbulent field – the wind field (v) – *is not* the direct result of a multiplicative cascade, that role is reserved for the energy flux (ε) which according to the dynamical (Navier Stokes) equations is (scale by scale) conserved by the nonlinear terms. On the contrary, the velocity field has fluctuations which follow:

$$\Delta v=\varepsilon^{f}\Delta x^{H};\quad f=1/3;\quad H=1/3 \tag{11}$$

where Δv is the fluctuation over a distance Δx and f, H are exponents determined in this case essentially by dimensional analysis. The exponent f is not so fundamental since if ε is a pure multiplicative cascade, then so is ε^{f} (this implies that if Z is a pure multiplicative process, and $Z=aR^{b}$, then the rain rate R is also a pure multiplicative cascade, although with different parameters). Since $\varepsilon^{f}=\lambda'^{\gamma}$ and taking $\Delta x=L=L_{\mathrm{eff}}/\lambda'$ we see that the effect of the extra Δx^{H} term is to shift the singularities: $\gamma\rightarrow\gamma-H$. The parameter H is called the “nonconservation parameter” since the ensemble average statistics follow $\langle\Delta v\rangle\approx\Delta x^{H}$ which – unless $H=0$ – implies that $<\Delta v>$ depends on the scale Δx. $H=0$ is thus a quantitative statement of scale by scale ensemble average conservation. Surveying the geophysical and turbulence literature, we find that empirically it is almost always the case that the observables have $H\neq0$, indeed they are almost always in the range $0<H<1$ (notable exceptions are the temperature and pressure in the vertical which have $H>1$, and $H\approx-0.35$ for rain rate in time on (climate) scales of one month and higher (Tessier et al., 1996).

Although there is no compelling theoretical reason for $H=0$ in rain (see however Lovejoy and Schertzer, in press for arguments to this effect), there have been surprisingly few attempts to estimate it empirically; the main exceptions are Tessier et al. (1993) who found $H=0.2\pm0.3$ in space (from sparse global raingage networks), Tessier et al. (1996) who found $H=-0.1\pm0.1$ in (daily, temporal) French rain gage rain rate estimates and De Lima (1998) who found −0.02 and −0.12 in time for various data sets with 15 min resolutions. These estimates have low accuracy due to the problems of sparse networks, accuracy of low rain rates, the annual cycle and other problems, however, they are apparently compatible with $H=0$. Note however that if there is a Marshall–Palmer type relation and $H=0$ for Z, then $H_R=0$ for the rain rate. However, it would be premature to conclude from our analysis that $H_R=0$.

The most direct way to estimate H is to directly determine the scaling of the fluctuations ΔZ. In the case where $0<H<1$, it is sufficient to use the standard structure function approach, i.e. to define the fluctuations by: $\Delta Z=|Z(x+\Delta x)-Z(x)|$, Fig. 13 shows the result $S(\lambda)=<\Delta Z(\Delta x)>$ with $\lambda=L_{\mathrm{earth}}/\Delta x$ (these are the first order structure functions; the more usual second order ones – variogrammes – could also be used but they would be much more intermittent). In the figure, we see a small deviation from the flat $H=0$ scaling for large λ (small Δx); however the comparison with the same analysis on the simulations shows that this small Δx effect is at least partially an artifact and that the spatial H is indeed very nearly 0 — probably to within about ±0.03, so that the reflectivity is nearly a pure multiplicative process. Since H was close to the lower limit of the structure function method, we also applied the Detrended Multifractal Fluctuation Analysis (DMFA) method (Kantelhart et al., 2002) which is valid for $-1<H<1$; we obtained nearly the same result.

Perhaps the most sensitive check that the value of H is near zero comes from comparing the $K(q)$ functions estimated from Z directly and from ΔZ at the finest resolution $\Delta x=L_{\mathrm{res}}$(denoted δZ; see Fig. 4E). To understand this, note that the effect of taking the absolute differences at the finest resolution is to remove the Δx^{H} term in Eq. (11) so that the singularities in δZ are shifted with respect to those of Z by an amount H. Therefore, the slopes $K'(q)$ of K_Z and $K_{\delta Z}$ differ by H. Fig. 14 shows the singularities estimated in the two different ways showing that except for the low q mostly affected by the minimum signal problem, that the difference is small; Fig. 14 shows that indeed, for $0.5<q<2$, $H=\Delta\gamma=0.00\pm0.01$; it also shows – using simulations – that at least in this range of q values which is not much affected by the minimum detectable signal – that with 10 simulated orbits – the method is accurate to about ±0.01. We thus conclude that $H=0.00\pm0.01$.

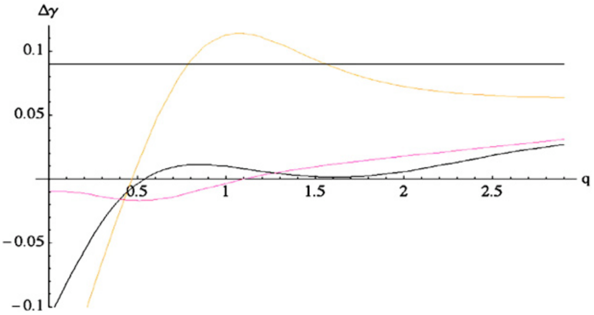

Fig. 14. The difference $\Delta\gamma$ in $\gamma(q)=K'(q)$ estimated from directly degrading the resolution of Z and by degrading the resolution of the absolute first differences in Z estimated at the finest resolution (δZ). The red is simulation with $H=0$ and threshold and black is the data. The orange line is the $\Delta\gamma$ obtained on a simulation with $H=0.09$, also thresholded. The flat black reference line is at the theoretical value 0.09 (all simulations had $a=1.5$, $C_1=0.63$, $Z_t=2<Z_1>$). (For interpretation of the references to color in this figure legend, the reader is referred to the web version of this article.)

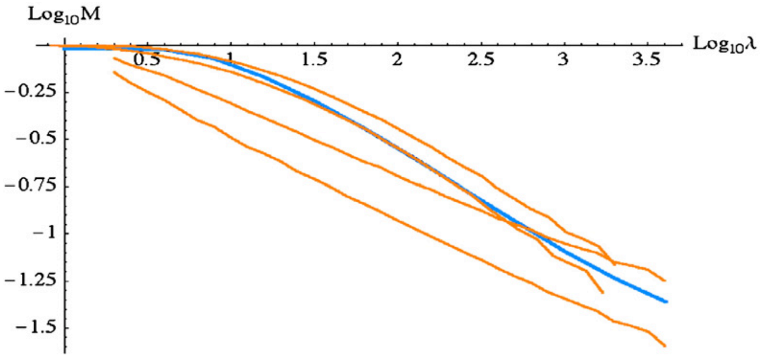

Fig. 15. This shows the $q=0$ curves for $\alpha=0.5$ (bottom), 0.8 (next up), data, (blue), $\alpha=1.5$ (close to the data) and then $\alpha=2$ (top). (For interpretation of the references to color in this figure legend, the reader is referred to the web version of this article.)

4.4. The multifractal index α

4.4.1. Low q, small Z behaviour and the minimum threshold

Using relatively straightforward estimation techniques, we have estimated the basic cascade sparseness parameter C_1 and the nonconservation parameter H. In addition the subsidiary parameters L_{eff} and $<Z_1>$ were also estimated, the former with some insight from simulations indicating that the $q=1.5$ moment is expected to be relatively well estimated. However, the index of multifractality α which determines the curvature of the $K(q)$ function (the rate at which the sparseness increases with intensity level), was "guesstimated" and the accuracy checked by simulation. Once α is given, then the minimum threshold Z_t is determined by the constraint that the apparent codimension of support $C_s=-K(0)$ gives the observed value 0.42, although – unsurprisingly – the value was always found to be about 20 *dBZ* i.e. the minimum detectable signal before the attenuation correction i.e. $Z_t\approx 2<Z_1>$. In Section 3.2, using the value $\alpha=1.5$ and $Z_t=2<Z_1>$, and simulating for 10 orbits, we saw that the small q curvature with scale is reasonably well reproduced, as well as the moments up to at least $q=2$, and we quantified the small deviations at about ±5% (Figs. 5, 9–11). However, until now, we did not attempt to justify this choice of α, and since we mentioned that the literature favors $\alpha\approx 0.5$ in time, but ≈1.3–1.5 in space (corresponding to multifractal processes with bounded or unbounded singularities respectively), it is necessary to examine this issue more closely.

Before turning to the large q, large Z statistics, we can already check that the low q statistics are indeed best reproduced by a model with $\alpha\approx 1.5$ combined with threshold such that $K(0)$ when estimated over the same range as the data ≈ -0.42. Fig. 15 shows the $q=0$ scaling of simulations for $\alpha=0.5$, 0.8, 1.5, 2 compared to the data. The left–right shift is fixed by the constraint that the $q=1.5$ moment have an external scale of 32,000 km. One sees that unlike the data and the $\alpha=1.5$, 2 values, the low α values are relatively straight and the curves are too low. On the contrary, the $\alpha=2$ curve is too high. More confidence in the estimate $\alpha\approx 1.5$ can be gained by considering the residuals over the entire range of q; this is shown in Fig. 16. Considering for the moment only the residuals for $q<1$, we see that the best fit is indeed obtained for $\alpha=1.5$. Since the smallness of the $q<1$ residuals will be affected by the details of the model used to reproduce the minimum detectable signal, it was not considered worthwhile to attempt to tune the α value any further.

4.4.2. The large q, extreme Z behaviour

While we have seen that the $\alpha=1.5$ model combined with the threshold model of the minimum detectable signal gives a reasonable approximation to the low q scaling, we have barely mentioned the large q behaviour which characterizes the statistics of the extreme reflectivities. This was partly justified by the fact that whereas ground and space based reflectivity statistics agreed quite well for moments $q<1$–1.2, (Fig. 4E) the ground based values had significantly higher exponents ($K(q)$) for $q>1.2$, possibly due to the relative absence of attenuation in the ground based data: in other words the high q TRMM statistics may not be so trustworthy.

In order to understand the large Z, large q TRMM statistics, recall that two attenuation correction methods are used, one based on a semi-empirical Z — attenuation coefficient relation (Hitschfeld and Bordan, 1954) and another method based on the surface reflection coefficient (Iguchi et al., 2000; Meneghini et al., 2000; Chiu and Shin, 2004). There is also a "beam filling" correction (Kozu and Iguchi, 1999) which attempts to partially account for the subpixel heterogeneity/fractality. These techniques have their limitations; for example in the large attenuation limit there will be no signal at all from the lower atmospheric layers, hence no signal to correct. Efforts to validate the TRMM data by comparing it to ground based radar have

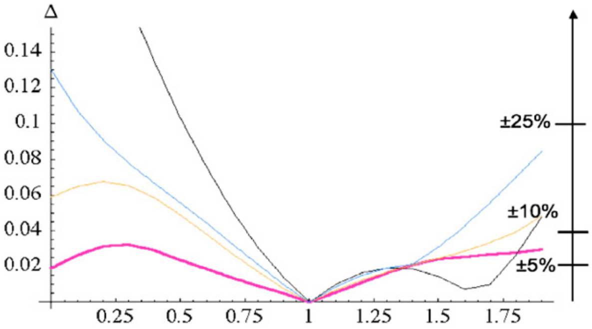

Fig. 16. Residuals of simulations with $a=0.5$ (black), 0.8 (blue), 1.5 (thick, purple), and 2 (orange). The simulations were constrained so that $C_s=-K(0)=0.42$ and the external scale for $q=1.5$ was 32,000 km. The corresponding percentages (obtained from $10^{\Delta-1}$) are also shown. (For interpretation of the references to color in this figure legend, the reader is referred to the web version of this article.)

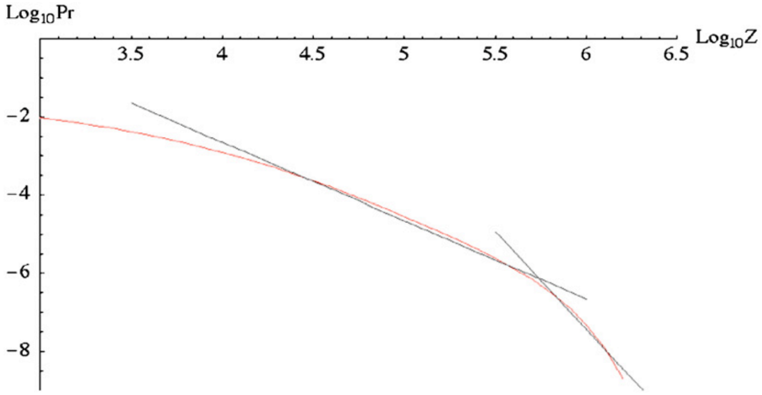

Fig. 17. The probability distribution from all the orbits (cumulated from Z to infinity: $\Pr(Z'>Z)$ where Z' is a randomly chosen reflectivity and Z is a threshold), reference slopes 2, 5, including zeroes.

systematically concluded on the contrary that the tendency is for the algorithm to slightly over-correct for attenuation at the highest reflectivity levels: (Liao et al., 2001; Amitai et al., 2004; Amitai et al., 2005). From graphs presented in Liao et al. (2001) it appears that this effect is mostly present for $dBZ>45$. While proper investigation of this effect may require the development of stratified 3D multifractal rain models, we can nevertheless study the statistics of the extremes in a bit more depth here.

Let us now consider the large q behaviour which is determined by the large singularities (γ, hence large Z values) corresponding to the extreme tail of the probability distribution of Z (hence large $c(\gamma)$, see Eqs. (7–9)). Fig. 17 shows the probability distribution of Z at the highest (4.3 km) resolution. Since $q=c'(\gamma)$, and $c'(\gamma)$ is proportional to the (negative) logarithmic derivative of the probability distribution, we find that the moment of order q is determined by the part of the curve in Fig. 17 with slope $=-q$. The reference lines in the figure show that the nearly linear region with slope roughly −2 starts at about 45 dBZ and extends to about 57 dBZ. This means that moments of order $2<q<5$ are predominantly determined by the rare Z values with probability $<10^{-6}$ (corresponding to a single reflectivity value every two orbits and with reflectivities >57 dBZ). According to the intercomparisons in Liao et al. (2001) these statistics may be significantly affected by the limitations of the attenuation correction technique; by its tendency to over correct.

To put this extreme behaviour in a scaling framework, we can calculate the codimension function $c(\gamma)$ which is a scale invariant probability distribution exponent. In Fig. 18 we estimate this two ways — directly from the probability distribution at the highest resolution ($c(\gamma)\approx-\log Z_\lambda/\log\lambda$)), and also from the Legendre transform of $K(q)$ (which is estimated over the full range of λ). We see that up until $c(\gamma)\approx1$, the two methods agree very well as expected if the scaling holds over the whole range. This implies that the scaling of the corresponding q's is good up to the same value. In order to make the correspondence, we display Fig. 19 which uses the Legendre transform to estimate $\gamma(q)=K'(q)$ and plots the corresponding $c(\gamma(q))$. We see that $c<1$ corresponds to moments $q<2$; we further see that c peaks at around 1.22 and then declines. Since theoretically for a pure scaling process, c must increase monotonically, this decrease is an artifact of the imperfect scaling of the high order moments ($q>2$–3) controlled by the very rare (and very large) Z values. This is a further indication that the moments $q>2$ may not be trustworthy. This spurious double valued-ness also explains the double valued-ness of the large γ behaviour in Fig. 18.

We can also use Fig. 19 to help understand the effect of sample size on the $K(q)$ function. For example we noted in Fig. 4D that as the sample size increases (one orbit, to one day (16 orbits) to the full set of orbits), that the $K(q)$ changes only very slightly. To understand the general effect of sample size, we note that in a space of dimension D, we cannot detect events with $c>D$ since that would imply impossible negative dimensions (recall $d(\gamma)=D-c(\gamma)$; $d(\gamma)$ is the fractal dimension corresponding to γ). Denoting the maximum order of singularity in the sample by γ_s, for a single $D=1$ section of the orbit, we expect $c(\gamma_s)=D=1$, (the swath width is small compared to the along track distance), this is roughly the effective dimension of a single orbit and provides another confirmation that only the corresponding moments $q<2$ are well determined from a single orbit. In order to understand what happens as we increase the sample size to 1 day and then to 2 1/2 months, denote by N_s the number of statistically independent realizations of the process over a range of

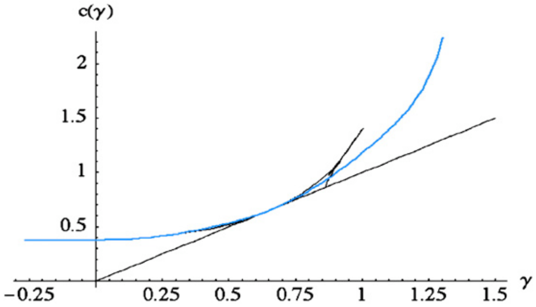

Fig. 18. $c(\gamma)$ calculated from probability distribution at the highest resolution (from Fig. 17, shown in blue) and from Legendre transform of $K(q)$, black. Note the double valued nature of the latter at large γ which is due to poor scaling at large q.

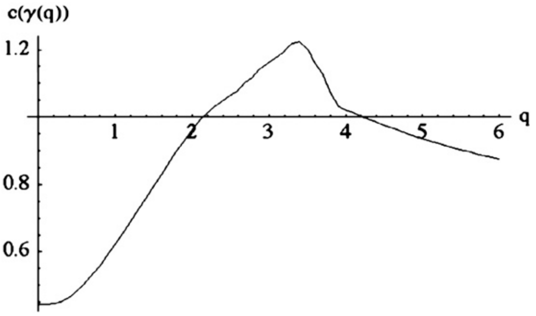

Fig. 19. This shows the $c(\gamma(q))$ showing how the qth order moment depends on the sample size. Since the sample size directly determines the maximum c which can be estimated (Eqs. (12), (13)), we can use this curve to understand how increasing the number of orbits will affect $K(q)$.

scales λ, and introduce the "sampling dimension" D_s. The precise result for the maximum singularity (Schertzer and Lovejoy, 1992) is:

$$c(\gamma_s) = D + D_s; \quad D_s = \frac{\log N_s}{\log \lambda'} \tag{12}$$

Since γ_s is the largest singularity in the sample (but not in the generating process which has N_s=infinity), to calculate the observed, finite sample $K(q)$, we must use the restricted Legendre transform:

$$K(q) = \max_{\gamma<\gamma_s}(q\gamma - c(\gamma)) = \begin{matrix} K(q); & q<q_s \\ q\gamma_s - c(\gamma_s); & q>q_s \end{matrix} \tag{13}$$

where $q_s = c'(\gamma_s)$ is the moment corresponding to γ_s i.e. $K(q)$ becomes spuriously linear for $q>q_s$, a "multifractal phase transition" (second order since $K''(q_s)$ is discontinuous).

From Fig. 19 we see that for $D_s>0.22$ (corresponding to $N_s\approx 7$ orbits here) that we do not expect any increase in γ_s, hence none in q_s; applying the above formulae for q_s allows us to explain the small change in $K(q)$ as we increase N_s. We conclude that $K(q)$ for $q<3$ will not change as N_s increases.

4.4.3. A possible explanation for the large q behaviour: divergence of moments and attenuation

We have argued that that the poor scaling implied by Fig. 19 for $q>2$–3 is probably due to inadequacies in the attenuation corrections at high rain rates applied to the TRMM data. We will now consider further the salient feature of Fig. 17 mentioned above: the relatively wide region with $\Pr\approx Z^{-2}$ behaviour extending roughly over the range 45–57 *dBZ* down to $\Pr\approx 10^{-6}$, implying that the second order moment barely converges if determined from a single orbit (which has $\approx 0.5\times 10^6$ pixels). Estimating the absolute logarithmic derivative (q_D) for the probability tail $Z>10^4$ mm^6/m^3 for each orbit yields $q_D=2.09\pm0.39$ which is indeed close to 2. The existence of such hyperbolic/algebraic probability tails is a generic consequence of multifractal cascade processes and arises from the singular small scale cascade limits. In order to understand this, one must distinguish "bare" and "dressed" cascade properties. The former refer to the statistics over cascades developed down to a given scale and stopped at that scale; the variability is purely due to the effects of the large scale. For the bare processes, all the moments are finite, Eq. (9) for $K(q)$ applies for all $q\geq 0$. However in the case where the cascade is continued down to infinitely small scales and then averaged at a finite intermediate scale, both the large and small scale variability are important. For these dressed properties, Eq. (9) only applies up to a critical moment order q_D after which the moments diverge. This implies that for the extreme fluctuations, the measured reflectivities (at scales much larger than the relaxation scale) follow the following hyperbolic form:

$$\Pr(Z>s)\approx s^{-q_D}; \quad s>>>1. \tag{14}$$

In the case of the TRMM data, it is possible that the unattentuated Z would continue the $\Pr\approx Z^{-2}$ behaviour asymptotically. Note that the fact that TRMM moments of order greater than about 2 depend on the extreme Z values indicates that the spectra – which is a second order moment – of Z will not converge well.

4.4.4. Consequences for K(q), and estimates of α

We may now compare the $K(q)$ functions obtained theoretically (infinite N_s, the bare process), with the actual numerical simulation of $K(q)$ (including the threshold effect); Fig. 20 shows this for α=0.5, 0.8, 1.5, 2. We first note that for $q<1$ the theoretical $K(q)$ are quite different from each other (and from the data), but that the simulations (which include the effect of thresholding) are very close to the data. Indeed, in Section 4.4.1 we saw that the chief difference between the different α values at the low q regime, were in the quality of the scaling after the thresholding: at low q, the low α values had quite good scaling whereas the larger α values had poor low q scaling (hence they were much closer to the data, Fig. 15). However, for large q the theoretical (bare) and simulated (dressed, finite sample) $K(q)$ are quite different from each other (see the thin lines in Fig. 20). This difference is because the simulations were over 10 orbits so that we expect the actual $K(q)$ to become linear as indicated. Indeed, because of this multifractal phase transition, even at large q, we do not see much difference between the empirical and the simulated $K(q)$ (for example using the theory Eqs. (12), (13) with $D_s\approx 0.3$ for the simulations we find that the asymptotic slope ($K'(q_s)=\gamma_s$) varies only a little: from 0.95 to 1.1 as α varies from 0.5 to 1.5; hence the simulated large q behaviour is not too different). In the absence of attenuation problems, we would expect the $K(q)$ for α=1.5 to become progressively steeper for

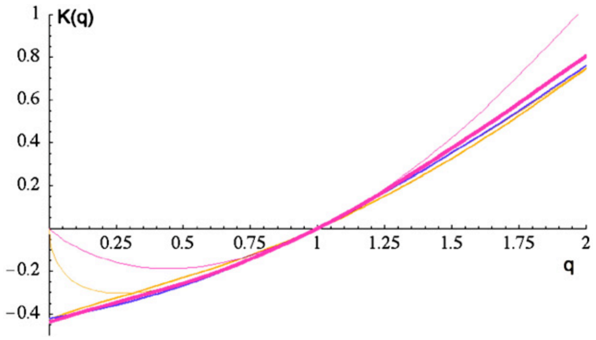

Fig. 20. The theoretical $K(q)$ for a=0.5 (thin orange line) and a=1.5 (thin red line). This is compared to the corresponding numerical simulations with threshold and only 10 orbits simulated (solid lines with the same color), as well as to the data (blue line). (For interpretation of the references to color in this figure legend, the reader is referred to the web version of this article.)

larger and larger sample sizes (increasing N_s, D_s, hence q_s, γ_s), so that to distinguish large and small α by considering the large q behaviour requires hypotheses about the latter (in particular, we must explain why $c(\gamma(q))$ reaches a spurious maximum, Fig. 19). The closeness of the simulations with $\alpha=0.5$ and $\alpha=1.5$ up to $q=2$ explains why the errors indicated in Fig. 16 are in fact quite comparable for both $\alpha=0.5$ and $\alpha=1.5$ (they are however substantially larger for $\alpha=2$).

Overall, considering both the small and large q behaviour and using the residuals (Fig. 16) as a criterion, we conclude that $\alpha\approx1.5$ is the optimum estimate. However, it should be borne in mind that this conclusion assumes a) that the threshold model is a good approximation to the actual minimum detectable signal, b) that the behaviour for $q>2$–3 is indeed an artifact (otherwise it turns out that the value $\alpha\approx0.6$ gives the best large q approximation to the observed $K(q)$).

5. The nature and modeling of the low and zero rain rates

5.1. Thresholding a pure cascade model, or a separate model for the support?

We have already mentioned the question of the zero rain rates: the fact that there are two simple models: the product of two processes (one of which determines the support, the other the rate) and a single process but with a physically determined threshold (the latter being an approximation to a more realistic compound multifractal–Poisson drop process). The fact that a strictly nonzero model coupled with a crude model of the minimum detectable signal leads to very close agreement with the empirical statistics shows that any physical threshold must be small. Let us therefore consider the implications of extrapolating the (unthresholded) model down to the small scale limit. Since the cascade clustering of the rain is largely the result of turbulent processes, we anticipate that the inner limit of the cascade is the scale at which the drops decouple from the turbulence due to their inertia; the decoupling scale where the turbulent Stokes number (the ratio of the inertial time of the drops to the turbulent eddy lifetimes) is unity (see Lovejoy and Schertzer, in press). This is indeed the conclusion that was reached in Lovejoy et al. (2003) and Lilley et al. (2006) on the basis of multifractal analyses of stereo photography of individual raindrops. More refined (spectral) analyses (Lovejoy and Schertzer, 2006b, in press) confirm that the transition decoupling scale L_c is in the range 30–50 cm (depending somewhat on the storm, rain rate), and that at scales smaller than this the rain follows a white noise spectrum while at larger scales, it follows a Corrsin–Obukhov (passive scalar, $k^{-5/3}$ spectrum, k is the wavenumber). Although the actual inner scale is in fact likely to be quite variable (determined by the local values of the particle number density, itself found to follow a k^{-2} spectrum) let us ignore this complication and consider for the moment that the inner scale is well defined and equal to 40 cm. In this case, in round numbers the relevant ranges of scale are: $L_{\mathrm{eff}}=40{,}000$ km, $L_{\mathrm{TRMM}}\approx4$ km, $L_c\approx0.4$ m. We therefore have a range of scale $\lambda=10^4$ down to the TRMM resolution; and another 10^4 down to L_c. Since the model is multiplicative, in order to extrapolate it over a range of scales of 10^4, (to obtain a model over a total range 10^8), we need only multiply each low resolution (4 km) pixel by an identical cascade reduced in size by 10^4.

Before doing this, let us examine a little more closely how accurately the thresholding reproduces the observed distribution of reflectivities. Fig. 21 shows the fraction of the area covered by rain as a function of the Z level for both a single orbit and for all the orbits. As expected, below about 20 mm^6/m^3, the data is (nearly) discontinuous whereas the simulation is continuous. The latter shows that even with a reflectivity sensitivity 1000 times lower than the mean (about 2000 times lower than at present), the TRMM radar would still only see rain over 29% of the region above this new minimum detectable level. To get a feel for the numbers, we can use the standard Marshall–Palmer Z–R relation (i.e. $Z=200\,R^{1.6}$), so that while the mean (53 mm^6/m^3) corresponds to 0.085 mm/h (at 4.3 km;

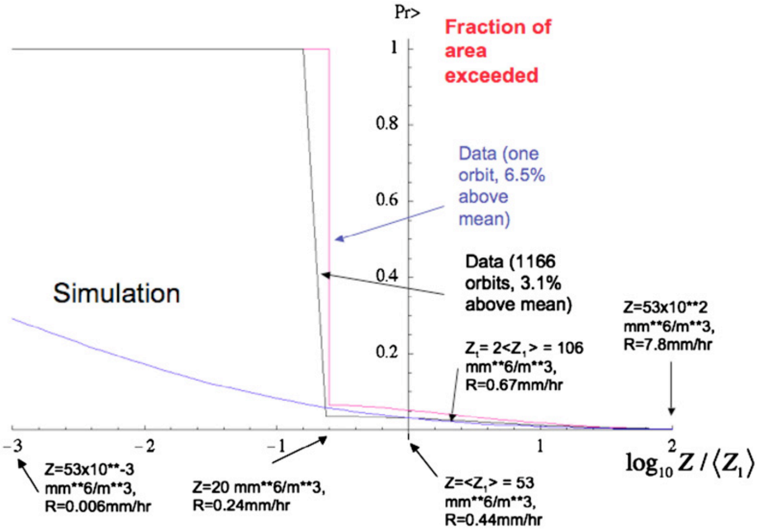

Fig. 21. The black is for all orbits, the pink for a single orbit, the blue for the simulations, all are normalized to have the same mean and the simulation has the same areal coverage at the mean (3.1% above the mean). At the far left we see that the simulation predicts that at a reflectivity level 1000 times lower than the mean (corresponding to 0.006 mm/h), there is still only 29% coverage by nonzero reflectivities.

Table 1

This table accompanies the schematic Fig. 22 and compares the reflectivities and (Marshall–Palmer *Z*–*R* inferred rain rates) at the TRMM scale (4.3 km) and the inner decoupling scale (take here as 40 cm)

	TRMM mean	Threshold 10^{-3} Z_1 (TRMM scale)	Decoupling scale	Threshold 10^{-3} Z_1 (decoupling scale)
Scale	4 km	4 km	0.4 m	0.4 m
Scale ratio	$\lambda_{\mathrm{TRRM}}=10^4$	$\lambda_{\mathrm{TRRM}}=10^4$	$\lambda_c=10^4=(\lambda_{\mathrm{TRRM}}=10^4)^2=10^8$	$\lambda_c=10^8$
Reflectivity (mm^6/m^3)	$\langle Z_1\rangle=53$	$Z_{\mathrm{TRMM,t}}=5.3\times10^{-2}$	$\langle Z_1\rangle=53$	$Z_{\mathrm{TRMM,t}}=5.3\times10^{-5}$
Rain rate mm/h	$\langle R_1\rangle=0.44$	$R_{\mathrm{TRMM,t}}=0.006$	$\langle R_1\rangle=0.44$	$R_{c,t}=10^{-4}\approx$ 0.7 mm/year
Fraction area exceeded	$F(>\langle Z_1\rangle)=F(>\langle R_1\rangle)=0.031$	0.29 (simulation)	$0.031^2=0.001$	$0.29^2=0.08$

Note that the mean rain rate (R_1(used here is obtained directly from (Z_1(; as pointed out in Section 1, it is 5.2 times larger than the mean obtained by converting *Z* to *R* at the finest resolution.

0.44 mm/h if the *Z*–*R* relation is applied at 20,000 km), the 2000 times more sensitive radar (at 4.3 km resolution) would "see" rain down to 0.006 mm/h. It's hard to know if this is realistic, but it underlines the fact that even in the absence of an additional threshold process the model predicts that almost all of the areas would have very low reflectivities/rain rates.

Let us now extrapolate this down to the decoupling scale. Using stereophotography of drops over roughly 10 m^3 regions, (Lovejoy et al., 2003; Lilley et al., 2006; Lovejoy and Schertzer, in press) showed that the scaling breaks down at a sub-metric decoupling scale where the drop inertia decouples them from the turbulence; they also estimated the universal multifractal parameters for *Z* as $C_1\approx0.21$, $\alpha=1.5$. This estimate was not considered too accurate since it was over a very small range of scales (about an octave) so that although the C_1 estimate is low, it is indeed possible that the scaling continues down to these small scales.

First consider the mean: since the cascade process is apparently conservative ($H=0$), if rain was measured at 40 cm scales, the mean would still be (53 mm^6/m^3); however, the fraction of the area exceeding the mean would be $0.031\times0.031\approx0.0009$, i.e. about 0.1% of the 40 cm×40 cm "pixels". However to extrapolate the values for a threshold 2000 times below the reflectivity mean, we must use the following:

$$Z_\lambda=\langle Z_1\rangle\lambda^\gamma \tag{15}$$

so that the threshold at $\lambda=10^4$ with $Z_\lambda/\langle Z_1\rangle=2000$ corresponds to a singularity of $\gamma\approx-3/4$. Using this value with $\lambda=10^8$ leads to $Z_{\lambda,t}=5.3\times10^{-5}$ mm^6/m^3 and a corresponding rain rate $R_{\lambda,t}=8\times10^{-5}$ mm/h i.e. about 0.7 mm/year (see Table 1 for summary, Fig. 22 for a schematic). However this low rain rate would be exceeded over a fraction of the area $=0.29^2\approx0.08$. The rate 0.7 mm/yr is so low that it corresponds to a single 1 mm diameter drop falling at ≈2 m/s in a volume of about 100 m^3. This may be close to the rain threshold we subjectively feel when walking outside at the "beginning" of a rain "event". It would mean that – even without a threshold – we would only subjectively "feel" rain 8% of the time, a number which seems surprisingly reasonable (recall that this is an average value over the TRMM region, i.e. ±38° latitude). If this is true, then the need for a minimum rain threshold becomes somewhat academic since it would only apply at these very low rain rates.

To put this in perspective, we have already noted that since $C_1=0.63$, the main contribution to the mean *Z* is at 14,600 mm^6/m^3; with the above numbers, using $C_{1R}=0.31$ (i.e. $b=1.6$, $\alpha=1.5$), we find that at 4.3 km resolution, the main contribution to the mean rain rate is 15.8 times the mean, i.e. 1.35 mm/h; at 40 cm resolution the corresponding rate is 24 mm/h.

5.2. Explaining various empirical features of radar estimates of rain

5.2.1. The area times constant technique for estimating areal rainfall

Over the past thirty years, there have been many techniques proposed for estimating areal rainfall. Many of these work by using ground based radar to estimate the areas of rain above the radar minimum threshold and then multiplying the result by a constant rate for raining areas.

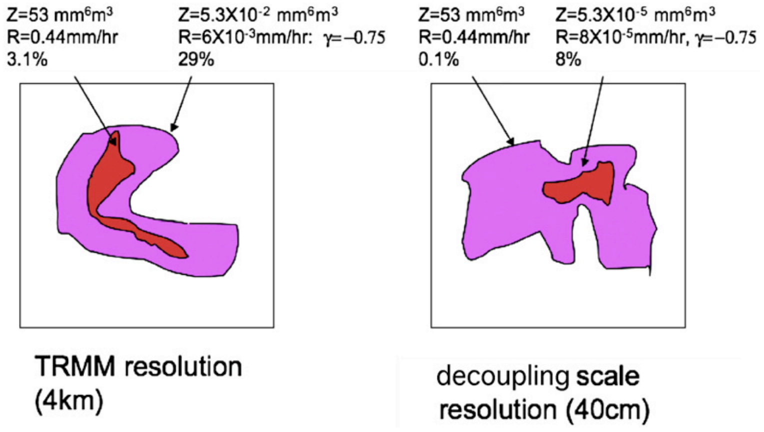

Fig. 22. This schematic indicates the implications of the model at inner "relaxation" scales and for very low reflectivities. The *Z*–*R* conversion uses the Marshall–Palmer relation which itself is only valid at most at a single scale so the *R* estimates are rough.

The “area times constant” technique (Lovejoy and Austin, 1979) and the “area-time integral” (Doneaud et al., 1984) technique are early examples of this (see also Krajewski et al., 1992). The GOES Precipitation Index (GPI; Arkin and Meisner, 1987) uses this basic idea to infer rain from areas defined by infra red radiance thresholds and the more sophisticated Adjusted GPI technique (AGPI, Huffman and Coauthors, 1997) is used with TRMM data to effectively extend the range of the TRMM radar with the help of visible and infra red instruments on the TRMM satellite (Adler et al., 2000).

To understand how area times constant type techniques work, we recall that the dominant contribution to the mean occurs at values of the field whose singularities are C_1. Using a Z–R relation we find that $C_{1R}=C_{1Z}b^{-\alpha}$ so that with $b=1.4$–1.6 and $C_{1Z}=0.63$ we find that $C_{1R}=0.38$–0.31; this quantifies the sparseness of the regions giving the dominant contribution to the mean rain rate. A necessary (but not sufficient) condition for an area times constant technique to work is thus that the area should have a codimension as close as possible to C_{1R} — otherwise the estimates of areal precipitation from the surrogate could not agree with the true rain field over any significant range of scales. We now note that with typical minimum detectable reflectivities that C_{1R} is close to the codimension of the support C_s; for the TRMM minimum detectable signal we found $C_s\approx 0.42$. This proximity of exponents (0.38, 0.42) shows that multiplying the support by a constant rate will give a rain rate estimate with the same scaling properties as the areal mean precipitation. More generally we see that the success of area times constant techniques depend on finding precipitation surrogates with supports C_s close to C_{1R}.

5.2.2. Spurious correlations between the dimensions of support and rain rates

Over and Gupta (1996a) and Gebremichael et al. (2006) have combined the area times constant idea with the scaling of the support of rain. They found empirically that the mean rain at 64–128 km scales is strongly correlated with the dimension of the support of rain D_s estimated over the range defined by this intermediate scale down to 4 km (in their notation $\tau_{OG}(0)=D_s=2-C_s$):

$$\tau_{OG}(0)=2-C_s=s\log\left(\frac{R_{\lambda_i}}{\langle R_1\rangle}\right)+i \tag{16}$$

where i is a constant, s is an empirical slope and λ_i is the ratio corresponding to the intermediate scale at which they calculate the local mean rain rate $R_{\lambda\iota}$. Taking $L_{\text{eff}}=32{,}000\approx 2^{15}$ km, we find that $\lambda_i=2^8$ corresponds to about 128 km or 32 TRMM pixels.

If $\tau_{OG}(0)$ (or equivalently C_s) was indeed a basic physically significant exponent, then the existence of a relation such as Eq. (16) would imply that the scaling could not hold at the larger scales (128 km and up, i.e. with ratio $<\lambda_i$). This is because in a scale invariant regime, the basic scaling exponents are independent of the rain rate; they simply determine the statistics of the latter. Indeed, in Gebremichael et al. (2006) the authors affirm – on the basis of regressions validating Eq. (16) – that indeed the TRMM scaling does not go to scales larger than about 128 km. However — in spite of the numerous scaling exponents they display, they do not show a single graph demonstrating any scaling whatsoever so that their conclusions about scaling are at best indirect.

However, we have seen that C_s is not a basic precipitation quantity at all; it is rather an artifact of the minimum detectable signal so that if Eq. (16) roughly holds, it must have a totally different explanation. Indeed, it is not hard to see how a rough relation of the type Eq. (16) might arise: whenever the intermediate scale mean $R_{\lambda i}$ is particularly large, only a small fraction of the sub 128 km pixels will have rain below the detection limit and C_s will tend to be small. On the contrary, whenever $R_{\lambda i}$ is particularly small there will be many sub 128 km pixels below the detectable level and C_s will tend to be large.

Using the model with parameters $\alpha=1.5$, $C_{1Z}=0.63$, $H=0$, $L_{\text{eff}}\approx 2^{15}$ km, it is easy to numerically simulate the (Gebremichael et al., 2006) results and show that they are in fact a *necessary consequence* of the wide range scaling coupled with an instrumental minimum detectable signal. Since they use a Z–R exponent $b=1.4$, we took the $1/b$ power of the Z used previously (equivalent to $C_{1R}=0.38$) as a model for R, and normalized it for their specific locations and times using their mean R which was about 0.7 mm/h, (about double the minimum detectable signal R_t at 4 km/pixel). Fig. 23 shows typical results for simulations of 256 regions, each with 32×32 pixels (4 km/pixel). We see that (similarly to their results) there is a lot of scatter but that the relationship is roughly linear. Quantitatively, we find the slope $s=0.24\pm 0.04$ where the error indicates the region to region variation due to stochastic cascade variability. This it is very close to the results of (Gebremichael et al., 2006) who find for six regions $s=0.22\pm 0.03$.

To have a rough understanding of this result, denote the minimum detectable signal R_t at highest scale ratio λ; take this as 2^{13}, corresponding to about 4 km. There is thus a minimum detectable singularity $\gamma_t=\log(R_t/\langle R_1\rangle)/\log\lambda$, an intermediate scale singularity $\gamma_i=\log(R_{\lambda\iota}/\langle R_1\rangle)/\log\lambda_i$ and — over the remaining range of factor $\lambda/\lambda_i=\lambda_s=2^5$ (down to 4 km), $\gamma_s=\log(R_{\lambda s}/\langle R_1\rangle)/\log\lambda_s$. If the intermediate ($\lambda_i$ scale) rain rate $R_{\lambda\iota}$ is given, then at a scale λ_s times

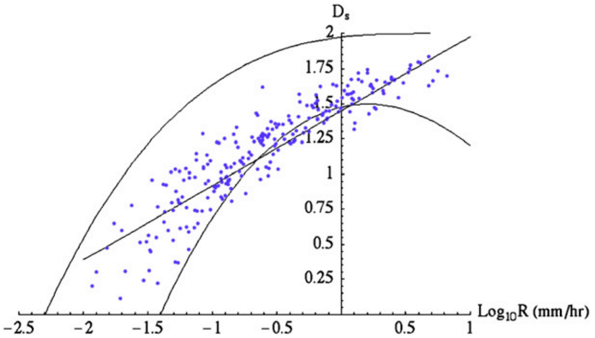

Fig. 23. This shows a simulation of the relation (for 256 regions) between the mean 128 km rain rate and the fractal dimension of the regions exceeding one half the mean rain rate (taken as 0.7 mm/h, roughly the same as in (Gebremichael et al., 2006). The straight line has slope corresponding to $s=0.23$, the curved lines are the rough bounds estimated theoretically below (note that following Gebremichael et al., 2006, s is defined using natural logs whereas the graph uses logs to base 10).

smaller (4 km) there will be a critical small scale singularity γ_{st} which will be at the detection limit. Due to the multiplicative nature of the cascade, these ratios and singularities satisfy:

$$\begin{aligned} &\Lambda = \lambda\lambda_{\mathrm{s}} \\ &\Lambda^{\gamma_{\mathrm{t}}} = \lambda_i^{\gamma_i}\lambda_{\mathrm{s}}^{\gamma_{\mathrm{st}}} \end{aligned} \tag{17}$$

for the scale ratios and singularities respectively. For a fixed intermediate scale λ_i rain rate singularity γ_i and detection limit singularity γ_t, we have from Eq. (17)

$$\gamma_{\mathrm{st}} = \gamma_{\mathrm{t}}\frac{\mathrm{Log}\,\Lambda}{\mathrm{Log}\,\lambda_{\mathrm{s}}} - \gamma_i\frac{\mathrm{Log}\,\lambda_i}{\mathrm{Log}\,\lambda_{\mathrm{s}}} \tag{18}$$

It is now easy to obtain bounds on the variation of C_{s} $(=2-\tau_{\mathrm{OG}}(0))$ as a function of γ_i $(R_{\lambda i})$. We can do this by exploiting the multiplicative nature of the cascade:

$$P \approx \lambda_{\mathrm{s}}^{-c(\gamma_{\mathrm{st}})}\lambda_i^{-c(\gamma_i)} \tag{19}$$

this equation just states that the probability P (fraction) of rain at the smallest scales at the detection limit is equal to the product of the probability (fraction) down to the intermediate scale ($\lambda_i^{-c(\gamma_i)}$) multiplied by the probability (fraction) over the last factor λ_{s} $(=\lambda_{\mathrm{s}}^{-c(\gamma_{\mathrm{st}})})$. When the singularities are related by Eq. (17) this is true because of the statistical independence of the different levels of the cascade. A simple approximation to the behaviour in Fig. 23 is now obtained by taking $P \approx \lambda_s^{-C_s}$ over the small scale range λ_{s} so that:

$$C_{\mathrm{s}}(\gamma_i) \approx c\left(\gamma_{\mathrm{t}}\frac{\mathrm{Log}\ \Lambda}{\mathrm{Log}\ \lambda_{\mathrm{s}}} - \gamma_i\frac{\mathrm{Log}\ \lambda_i}{\mathrm{Log}\ \lambda_{\mathrm{s}}}\right) + c(\gamma_i)\frac{\log\ _{\lambda i}}{\log\ \lambda_s} \tag{20}$$

In Fig. 23 we show $D_{\mathrm{s}}=2-C_{\mathrm{s}}=\tau_{\mathrm{OG}}(0)$; we see that it tends to under-estimate the correct behaviour, but follows it quite well. Also shown in the figure is an upper bound obtained by considering that the intermediate scale is space filling ($c(\gamma_i)\approx 0$) so that $C_{\mathrm{s}} \approx (\gamma_{\mathrm{st}})$ (i.e. ignoring the second term in Eq. (20)). We can also see that the value of s is apparently well approximated by the derivative — $C_{\mathrm{s}}'(0)$ i.e. when evaluated at the mean rain rate.

5.2.3. Deviations from scale invariance

We mentioned that Gebremichael et al. (2006) interpreted the relation between C_{s}, $R_{\lambda i}$ as a breakdown in the scaling — rather than as a consequence of it. However, rather than directly testing the scaling as we have done here, they hypothesized the following ad hoc form for possible deviations from the scaling:

$$\log\left(\frac{\langle R_{2\lambda}^q\rangle}{\langle R_\lambda^q\rangle}\right) = K(q)\log 2 + \chi(q)\log\lambda \tag{21}$$

where $\chi(q)$ $\log\lambda$ is their ad hoc nonscaling term. Using a cascade model which was taken to be a product of the $\alpha=0$ and $\alpha=2$ universal multifractals, (but with the parameters estimated without taking into account the large biases due to the minimum detectable signal: their σ^2 parameter is 2.65 times too small, see Section 3.1), they were able to sometimes statistically reject the hypothesis that $\chi(0)$ and $\chi(2)$ are nonzero. However, it is important to realize that – as usual in statistical hypothesis testing – rejecting the hypothesis that $\chi\neq 0$ in no way requires us to accept the converse (i.e. that $\chi=0$, and hence that scaling is respected). The fact that authors are frequently unable to reject the hypothesis that $\chi(0)$ and $\chi(2)$ are nonzero may simply indicate that they have made a poor choice of the ad hoc nonscaling ansatz. We conclude that failure to reject the hypothesis that $\chi\neq 0$ says nothing about either the scaling or the nonscaling ansatz: no matter what the outcome of their statistical tests, we are none the wiser about the quality of the pure scaling form Eq. (1).

Finally it is also worth mentioning that the scale invariance of the precipitation process could lead to scaling corrections to the pure power law form (Eq. (1)) e.g. involving logarithms, iterated logarithms etc. This is investigated in satellite radiances in Lovejoy and Schertzer (2006a).

6. Conclusions

In the absence of direct information, the scale by scale nature of atmospheric dynamics in general – and rain in particular – has been the subject of competing theories and approaches. On the one hand, the dynamical meteorology approach has attempted to phenomenologically distinguish different dynamical mechanisms each postulated to dominate over narrow ranges of scale. This view identifies form with mechanism and treats atmospheric dynamics as a hierarchy of different phenomena each dominating a different range of scales. In comparison, the classical turbulence based model — which postulates isotropic three dimensional turbulence at small scales and isotropic two dimensional turbulence at large scales (with the two separated by "meso-scale gap" in the spectrum) is more parsimonious, but makes its own strong a priori assumptions; in this case that the turbulence is isotropic. State of the art drop sonde (Lovejoy et al., 2007) and lidar analyses (Lilley et al., 2004) show that on the contrary the turbulence is strongly anisotropic (with different scaling exponents in the horizontal and vertical directions implying that the atmospheric stratification is scaling. If the atmosphere is indeed an anisotropic scaling system then the small roundish structures correspond – when anisotropically "blown up" in scale – to large flattened structures. Contrary to the phenomenological assumptions, the appearance of structures changes with scale even though the underlying mechanism does not. This illustrates the "phenomenological fallacy" (Lovejoy and Schertzer, 2007) of identifying appearance with mechanism. Since the large scale "blowups" of small roundish eddies (in rain, "cells") can be flat and stratified (in rain, "stratiform"), scaling stratification allows the possibility of wide range scaling of atmospheric processes in general, and of rain in particular.

While the anisotropic turbulent approach was verified twenty years ago in rain up to ≈100 km (Lovejoy et al., 1987; Schertzer and Lovejoy, 1987) direct confirmation that it extended up to planetary scales has been lacking. The closest evidence to date – up to scales of 5000 km – were from geostationary visible and infra red satellite radiances (which are correlated with the rain) (Lovejoy et al., 2001; Lovejoy and Schertzer, 2006a). In this paper, we exploit space borne (TRMM) radar to directly confirm that reflectivities from rain are scaling up to planetary scales. The TRMM radar gives a relatively uniform high quality attenuation-corrected reflectivity map, whose main limitation is the relatively large minimum detectable signal and the limitations of the attenuation corrections at very high reflectivities. We deliberately avoided consideration of the more problematic rain rate estimates. Statistical moments with order q in the range $0<q<2$ (corresponding to all reflectivities except the extremes with probabilities $<10^{-6}$) give remarkably good scaling: ±6.4%, for the reflectivity and ±4.3% for the reflectivity increments over the directly observed entire range 20,000 down to 4.3 km (Fig. 4A, B, >1100 consecutive orbits ≈75 days). Nonetheless, there are small but systematic deviations, particularly for the low order moments which are sensitive to the presence of reflectivities below the detection limit (which is about twice the mean i.e. about 20 *dBZ*).

Imposing a threshold on a rain process at a fixed scale breaks the scaling. In order to see how well this might explain the remaining small deviations from scaling at small q values, a simple threshold model for the minimum detectable signal was used in conjunction with a stochastic (multifractal) cascade model of the reflectivity. Since we fit a stochastic model (not simply determine regression parameters), the model parameters were estimated using a "bootstrap" procedure; we concluded that a universal multifractal model with fundamental parameters $\alpha=1.5$, $C_1=0.63\pm0.02$, $H=0.00\pm0.01$ was reasonable. Although the value $\alpha=1.5$ had significantly lower residuals than $\alpha=0.5$, 0.8 or $\alpha=2$, we did not attempt a precise error estimate since such an estimate would be sensitive to both the small Z modeling of the minimum signal and the large Z modeling of the attenuation correction. In addition, there were three secondary parameters: the mean (climatological) reflectivity $<Z_1>=53$ mm^6/m^3 (17 *dBZ*), the detection threshold $Z_t,=2<Z_1>$ (20 *dBZ*) and the effective outer scale of the cascade, $L_{\mathrm{eff}}=32{,}000\pm2000$ km. With this model, we found the mean residual between the model and data was less than ±4.6% for the entire range down to 4.3 km and for the moments $q\leq2$. Since the bootstrap was somewhat crude, this residual is an upper bound on the true residual. The smallness of these deviations from universal multifractal scale invariance shows that the latter is one of the most accurately obeyed laws in atmospheric science, comparable in accuracy to the routinely used hydrostatic approximation (±≈2%) and close to the exponential decay law for atmospheric pressure (±≈1%). Indeed, it is remarkable that the strong long range statistical dependencies that it implies have not yet been exploited either for rain rate estimation or for meteorological forecasting (see however Schertzer and Lovejoy, 2004 for stochastic forecasting; the TRMM temporal scaling will be studied in future publications). The reason for this may be the increasing tendency for new sources of data to be exclusively used for making "products" rather than for answering fundamental scientific problems, or for developing ad hoc algorithms before their theoretical and empirical bases have been examined.

Two salient points need additional comment. First, we directly estimated the scale by scale conservation parameter H which quantifies the deviation of the process from a pure multiplicative one; we found it was very near zero (the small deviations could be explained by the model). Although $H=0$ is almost always assumed for rain, it has never been accurately estimated before (note that if Marshall–Palmer type relations hold, the value $H=0$ for the reflectivity would imply $H_R=0$ for the rain rate). A second comment concerns the fact that the effective outer scale L_{eff} is somewhat larger than the planetary scale. The ratio $L_{\mathrm{eff}}/L_{\mathrm{earth}}\approx1.6$ is a measure of the variability of planetary size rain structures. This value is compatible with those obtained by extrapolations of ground based radar (by a factor of 300 or so in scale). Finally, the most difficult parameter to estimate, the multifractal index was estimated at $\alpha\approx1.5$ by comparing simulations with higher and lower α's and considering small q deviations due to thresholding, and large q deviations due to (presumably) attenuation effects.

A remarkable feature of the agreement between the stochastic cascade model and the reflectivity data is that the pure cascade (unthresholded) model implies a nonzero rain rate everywhere. This is brings up the longstanding "zero rain rate" problem (Larnder, 1995; Marsan et al., 1996): which has most often been resolved in an ad hoc manner by simply postulating separate (and independent) processes for the support of rain and for the rain rate on the support. The alternative is simply to put a low threshold on the rain process (this is in fact an approximation to a compound multifractal Poisson process). While our findings do not fully resolve the issue, they do show that the debate may be fairly academic: if the model is extrapolated down to the inner decoupling scale (where the drops and turbulence decouple — where the Strokes number is unity — typically about 40 cm), then it predicts that for data at 40 cm scales, that rates above ≈1 mm/year will only occur about 8% of the time. Since this low rate is probably close to the subjective rain/no rain threshold, this indicates that even without a physical threshold, we would only subjectively experience rain about 8% of the time (this is an average over all the TRMM region, ±38° latitude). In any case, if a physical rain/no rain threshold exists, it must be very small and neglecting it may not lead to significant error.

The model also explains several features of rain statistics, including the relative success of area times constant techniques for estimating areal rainfall. We saw that the key is to choose a surrogate for rain whose support has codimension $C_s\approx C_{1R}$. If this condition is not satisfied then the scaling of the surrogate and the areal rainfall will be different so that agreement will necessarily be poor. The requirement that C_s for a surrogate $=C_{1R}$ could potentially lead to improvements in GPI, AGPI and related visible/IR techniques. This is an application of the idea of stochastic calibration which could also be applied to rain gauge/radar calibration: i.e. the fact that radar rain and rain gauge rain must have the same scale by scale statistics (i.e. same scaling exponents). We also saw how instrumental minimum detectable signals combined with wide range scaling leads to roughly log linear rain rate — C_s relations at intermediate (e.g. 128 km) scales. The existence of such spurious (instrument induced) relations therefore supports the wide range scaling of rain contrary to (Gebremichael et al., 2006) who interpreted it as a breakdown in the scaling.

The confirmation that cascade processes can accurately explain rain reflectivity statistics down to 4 km scales has implications for the way we convert reflectivities into rain rate estimates. First, it implies that any Z–R relation must be statistical — not one-to-one as is usually assumed. This is because while the reflectivity is the integral of the drop volumes squared, the rain rate is the integral of the volumes multiplied by the vertical fall speeds, the latter depending notably on the wind field (and hence on the wind–rain coupling). Second, the statistical relation will be scale dependent: due to the scaling it will vary in a power law way with the space-time resolution of the radar. Indeed, one will probably need detailed stochastic coupled turbulence–drop models (perhaps of the compound multifractal/Poisson type proposed in Lovejoy and Schertzer, 2006b) in order to fully clarify the relation. The development of such models will undoubtedly help to settle longstanding debates about "radar calibration" including those surrounding TRMM validation.

Acknowledgements

We thank Alexandre Radkevitch, Alin Carsteanu and Eric Smith for helpful discussions. This research was for carried out for scientific purposes only, it was unfunded.

References

Adler, R.F., et al., 2000. Tropical rainfall distributions determined using TRMM combined with other satellite and rain gauge information. J. Appl. Meteor. 39, 2007–2023.

Amitai, E., et al., 2004. Uniting space, ground and underwater measurements for improved estimates of rain rate. IEEE Geosci. and Remote Sens. Lett. 1, 35–38.

Amitai, E., et al., 2005. Accuracy verification of spaceborne radar estimates of rain rate. Atmos. Sci. Lett. 6, 2–6. doi:10.1002/asl.1082.

Anselmet, F., Antonia, R.A., Danaila, L., 2001. Turbulent flows and intermittency in laboratory experiments. Plan. Space Sci. 49, 1177–1191.

Arkin, P.A., Meisner, B.N., 1987. The relationship between largescale convective rainfall and cold cloud over the Western Hemisphere during 1982–1984. Mon. Weather Rev. 115, 51–74.

Bendjoudi, H., Hubert, P., Schertzer, D., Lovejoy, S., 1997. Interprétation multifractale des courbes intensité-durée-fréquence des précipitations, Multifractal point of view on rainfall intensity-duration-frequency curves, C.R. A. S. Sciences de la terre et des planetes/Earth Planet. Sci. 325, 323–326.

Chiu, L., Shin, B.D., 2004. Monthly Surface Rain Rate from TRMM Algorithms: Annual Mean Comparison, Paper Presented at 35th COSPAR Scientific Assembly. Held 18 - 25 July, Paris, France.

De Lima, I. (1998), Multifractals and the temporal structure of rainfall, PhD thesis, 225 pp, Wageningen.

Deidda, R., 2000. Rainfall downscaling in a space-time multifractal framework. Water Resour. Res. 36, 1779–1794.

Deidda, R., et al., 2004. Space-time scaling in high intensity tropical ocean global atmosphere coupled ocean-atmosphere response experiment (TOGA-COARE) storms. Water Resour. Res. 40, W02506. doi:10.1029/02003WR002574.

Doneaud, A.A., et al., 1984. The area-time integral as an indicator for convective rain volumes. J. Clim. Appl. Meteorol. 23, 555–561.

Fraedrich, K., Larnder, C., 1993. Scaling regimes of composite rainfall time series. Tellus 45 A, 289–298.

Frisch, U., et al., 1978. A simple dynamical model of intermittency in fully develop turbulence. J. Fluid Mech. 87, 719–724.

Gebremichael, M., et al., 2006. Comparison of the scaling characteristics of rainfall derived from space-based and ground-based radar observations. J. Hydrometeor. 7, 1277–1294.

Gupta, V.K., Waymire, E., 1990. Multiscaling properties of spatial rainfall and river distribution. J. Geophys. Res. 95, 1999–2010.

Gupta, V.K., Waymire, E., 1991. On lognormality and scaling in spatial rainfall averages? In: Schertzer, D., Lovejoy, S. (Eds.), Non-Linear Variability in Geophysics: Scaling and Fractals. Kluwer, pp. 175–184.

Gupta, V.K., Waymire, E., 1993. A statistical analysis of mesoscale rainfall as a random cascade. J. Appl. Meteorol. 32, 251–267.

Halsey, T.C., et al., 1986. Fractal measures and their singularities: the characterization of strange sets. Phys. Rev. A 33, 1141–1151.

Harris, D., et al., 1996. Multifractal characterizastion of rain fields with a strong orographics influence. J. Geophys. Res. 101, 26405–26414.

Hitschfeld, W., Bordan, J., 1954. Errors inherent in the radar wavelength measurement of rainfall at attenuating wavelengths. J. Meteorol. 11, 58–67.

Hogan, R.J., Kew, S.F., 2005. A 3D stochastic cloud model for investigating the radiative properties of inhomogeneous cirrus clouds. Q. J. R. Meteorol. Soc. 131, 2585–2608.

Hubert, P., Carbonnel, J.P., 1988. Caracterisation fractale de la variabilité et de l' anisotropie des precipitations tropicales. Comptes Rendus de l'Académie des Sciences de Paris 2, 909–914.

Hubert, P., Carbonnel, J.P., 1989. Dimensions fractales de l' occurence de pluie en climat Soudano-Sahélien. Hydrol. Cont. 4, 3–10.

Hubert, P., Carbonnel, J.P., 1991. Fractal characterization of intertropical precipitations variability and anisotropy. In: Schertzer, D., Lovejoy, S. (Eds.), Non-Linear Variability in Geophysics: Scaling and Fractals. Kluwer, pp. 209–213.

Hubert, P., et al., 1993. Multifractals and extreme rainfall events. Geophys. Res. Lett. 20, 931–934.

Hubert, P., Bendjoudi, H., Schertzer, D., Lovejoy, S., 1995. Fractals et mulitfractals appliqués à l'étude de la varaibilité temporelle des précipitations. In: Feddes, R.A. (Ed.), Space and Time Scale Variability and Interdependencies in Hydrological Processes. Cambridge University press, Cambridge, pp. 175–181.

Huffman, G.J., Coauthors, 1997. The Global Precipitation Climatology Project (GPCP) combined precipitation dataset. Bull. Am. Meteorol. Soc. 78, 5–20.

Iguchi, T., et al., 2000. Rain-profiling algorithm for the TRMM precipitation radar. J. Appl. Meteorol. 39, 2038–2052.

Kantelhart, J.W., et al., 2002. Multifractal detrended fluctuation analysis of nonstationary time series. Physica A 316, 87–114.

Kozu, T., Iguchi, T., 1999. Nonuniform beamfilling correction for spaceborne radar rainfall measurement: implication from TOGA COARE radar data analysis. J. Atmos. Ocean. Technol. 16, 1722–1735.

Krajewski, W.F., et al., 1992. The accuracy of the area-threshold method: a model-based simulation study. J. Appl. Meteorol. 31, 1396–1406.

Kumar, P., Foufoula-Georgiou, E., 1993. A new look at rainfall fluctuations and scaling properties of spatial rainfall. J. Appl. Meteorol. 32, 2.

Larnder, C. (1995), Observer problems in multifractals: the example of rain, MSc. thesis, 105 pp, McGill, Montreal.

Liao, L., et al., 2001. Comparisons of rain rate and reflectivity factor derived from the TRMM precipitation radar and the WSR-88D over the Melbourne, Florida Site. J. Atmos. Ocean. Technol. 18, 1959–1974.

Lilley, M., et al., 2004. 23/9 dimensional anisotropic scaling of passive admixtures using lidar aerosol data. Phys. Rev. E 70, 036301–036307.

Lilley, M., et al., 2006. Multifractal large number of drops limit in Rain. J. Hydrol. 328, 20–37.

Lopez, R.E., 1979. The log–normal distribution and cumulus cloud populations. Mon. Weather Rev. 105, 865–872.

Lovejoy, S., 1982. Area perimeter relations for rain and cloud areas. Science 187, 1035–1037.

Lovejoy, S., Austin, G.L., 1979. The sources of error in rain amount estimating schemes from GOES visible and IR satellite data. Mon. Weather Rev. 107, 1048–1054.

Lovejoy, S., Schertzer, D., 1985. Generalized scale invariance and fractal models of rain. Water Resources Research 21, 1233–1250.

Lovejoy, S., Schertzer, D., 1995. Multifractals and rain. In: Kunzewicz, Z.W. (Ed.), New Uncertainty Concepts in Hydrology and Water Resources. Cambridge University Press, pp. 62–103.

Lovejoy, S., Schertzer, D., 2006a. Multifractals, cloud radiances and rain. J. Hydrol. 322, 59–88.

Lovejoy, S., Schertzer, D., 2006b. Stereophotography of rain drops and compound Poisson — cascade processes, paper presented at cloud conference. American Meteor. Soc., Madison, Wi. July 12–14, pp. 14.4.1–14.4.19.

Lovejoy, S., Schertzer, D., 2007. Scale, scaling and multifractals in geophysics: twenty years on. In: A.A. Tsonis, J.E. (Ed.), Nonlinear dynamics in geophysics. Elsevier.

Lovejoy, S., Schertzer, D., in press. Turbulence, rain drops and the $l^{1/2}$ number density law. New J. Phys.

Lovejoy, S., et al., 1986. Fractal characterisation of inhomogeneous measuring networks. Nature 319, 43–44.

Lovejoy, S., et al., 1987. Functional sbox-counting and multiple dimensions in rain. Science 235, 1036–1038.

Lovejoy, S., et al., 1996. The scalar multifractal radar observer's problem. J. Geophys. Res. 31D, 26,479–426,492.

Lovejoy, S., Schertzer, D., Stanway, J.D., 2001. Direct evidence of planetary scale atmospheric cascade dynamics. Phys. Rev. Lett. 86, 5200–5203.

Lovejoy, S., et al., 2003. Large particle number limit in Rain. Phys. Rev. E 68, 025301.

Lovejoy, S., et al., 2007. Is isotropic turbulence relevant in the atmosphere? Geophys. Res. Lett. 34, L14802. doi:10.1029/2007GL029359.

Lovejoy, S., Schertzer, D., Allaire, V., Bourgeois, T., King, S., Pinel, J., Stolle, J., submitted for publication. Atmospheric complexity or scale by scale simplicity? Phys. Rev. Lett. (January).

Marsan, D., et al., 1996. Causal space-time multifractal processes: predictability and forecasting of rain fields. J. Geophys. Res. 31D, 26,333–326,346.

Menabde, M., Harris, D., Seed, A., Austin, G., Stow, D., 1997. Multiscaling properties of rainfall and bounded random cascades. Water Resour. Res. 33, 2823–2830.

Meneghini, R., et al., 2000. Use of the surface reference technique for path attenuation estimates from the TRMM precipitation radar. J. Appl. Meteorol. 39, 2053–2070.

Olsson, J., 1995. Limits and Characteristics of the Multifractal Behavior of a High-Resolution Rainfall Time Series. non-linear processes in geophysics, vol. 2, pp. 23–29.
Olsson, J., et al., 1990. Fractal properties of rainfall. Ann. Geophys. 142 special issue.
Olsson, J., et al., 1993. Fractal analysis of high resolution rainfall time series. J. Geophys. Res. 98, 23265–23274.
Over, T., Gupta, V.K., 1996a. A space-time theory of mesoscale rainfall using random cascades. J. Geophys. Res. 101, 26319–26331.
Over, T.M., Gupta, V.K., 1996b. A space-time theory of mesoscale rainfall using random cascades. J. Geophys. Res. 101 (D21), 26,319–326,331.
Over, T.M., Gupta, V.K., 1996c. Statistical analysis of mesoscale rainfall: dependence of a random cascade generator on large scale forcing. J. Appl. Meteorol. 33, 1526–1542.
Parisi, G., Frisch, U., 1985. A multifractal model of intermittency. In: Ghil, M., et al. (Ed.), Turbulence and Predictability in Geophysical Fluid Dynamics and Climate Dynamics. North Holland, Amsterdam, pp. 84–88.
Schertzer, D., Lovejoy, S., 1987. Physical modeling and analysis of rain and clouds by anisotropic scaling of multiplicative processes. J. Geophys. Res. 92, 9693–9714.
Schertzer, D., Lovejoy, S., 1992. Hard and soft multifractal processes. Physica A 185, 187–194.
Schertzer, D., Lovejoy, S., 1997. Universal multifractals do exist! J. Appl. Meteorol. 36, 1296–1303.
Schertzer, D., Lovejoy, S., 2004. Uncertainty and predictability in geophysics: chaos and multifractal insights. In: Sparks, R.S.J., Hawkesworth, C.J. (Eds.), State of the Planet, Frontiers and Challenges in Geophysics. American Geophysical Union, Washington, pp. 317–334.
Schertzer, D., Lovejoy, S., Lavallée, D., 1993. Generic multifractal phase transitions and self-organized criticality. In: Perdang, J.M., Lejeune, A. (Eds.), Cellular Automata: prospects in astrophysical applications. World Scientific, pp. 216–227.
Schmitt, F., et al., 1992. Empirical determination of universal multifractal exponents in turbulent velocity fields. Phys. Rev. Lett. 68, 305–308.
Tessier, Y., et al., 1993. Universal multifractals: theory and observations for rain and clouds. J. Appl. Meteorol. 32, 223–250.
Tessier, Y., et al., 1994. The multifractal global raingage network: analysis and simulation. J. Appl. Meteorol. 32, 1572–1586.
Tessier, Y., et al., 1996. Multifractal analysis and modeling of rainfall and river flows and scaling, causal transfer functions. J. Geophy. Res. 31D, 26,427–426,440.
TRMM Precipitation Radar Team, J. A. E. A. J., National Aeronautics and Space Administration (NASA), 2005. Tropical Rainfall Measuring Mission (TRMM), Precipitation Radar Algorithm Instruction Manual For Version 6. NASA. 180 pp., JAXA.
Veneziano, D., et al., 1996. Nonlinearity and self-similarity of rainfall in time and a stochastic model. J. Geophys. Res. 101, 26371–26392.
Venugopal, V., et al., 2006. Revisiting multifractality of high-resolution temporal rainfall using a wavelet-based formalism. Water Resour. Res. doi:10.1029/2005WR004489.